Atomistic Molecular Dynamics Simulation and COSMO-SAC Approach for Enhanced 1,3-Propanediol Extraction with Imidazolium-Based Ionic Liquids

Raj Akshat
Birla Institute of Technology, Mesra
Anand Bharti
Birla Institute of Technology, Mesra
Padmini Padmanabhan (padmini@bitmesra.ac.in)
Birla Institute of Technology, Mesra

Research Article

Keywords: 1,3-Propanediol, Ionic liquids, Molecular dynamics, COSMO-SAC

Posted Date: January 19th, 2024

DOI: https://doi.org/10.21203/rs.3.rs-3852183/v1

Additional Declarations:
No competing interests reported.

Tables are available in the Supplementary Files section.

Atomistic Molecular Dynamics Simulation and COSMO-SAC Approach for Enhanced 1,3-Propanediol Extraction with Imidazolium-Based Ionic Liquids

Raj Akshat[a], Anand Bharti[b*] and Padmini Padmanabhan[a*]

[a]*Department of Bioengineering and Biotechnology, Birla Institute of Technology, Ranchi, India*

[b]*Department of Chemical Engineering, Birla Institute of Technology, Ranchi, India*

* Corresponding author:

E-mail: abharti@bitmesra.ac.in, padmini@bitmesra.ac.in

ABSTRACT

1,3-Propanediol (1,3-PDO) holds significant industrial importance, but its eco-friendly extraction remains a challenge. To address this, we investigated the performance of four ionic liquids ([Bmim][NTF2], [Bmim][NPF2], [Bmim][SCN], and [Bmim][TFO]) via Molecular Dynamics simulations for 1,3-PDO extraction.

Analysis of radial distribution functions (RDF) and spatial distribution functions (SDF) demonstrated enhanced 1,3-PDO coordination around [Bmim][SCN], with higher density in [Bmim][SCN] and [Bmim][TFO] compared to [Bmim][NPF2] and [Bmim][NTF2]. [Bmim][TFO] and [Bmim][SCN] exhibited pronounced RDF anion peaks, indicating robust hydrogen bonding interactions and a higher concentration of 1,3-PDO around them. [Bmim][SCN] formed the highest number of hydrogen bonds (1.639) due to its coordinating [SCN]- anion, which bonded with 1,3-propanediol's [OH]- groups. In contrast, non-coordinating anions in [Bmim][NPF2] and [Bmim][NTF2] formed fewer hydrogen bonds. Within a ternary system, [Bmim][SCN] and [Bmim][TFO] excelled at 1,3-PDO extraction, surpassing [Bmim][NPF2] and [Bmim][NTF2] with selectivity around 29. Anion variations significantly influenced distribution coefficients and selectivity values.

COSMO-SAC, a predictive thermodynamic model, confirmed 1,3-PDO's strong interaction with [Bmim][SCN] and [Bmim][TFO]. This study enhances our understanding of IL-1,3-PDO systems and their potential in eco-friendly extraction processes. [Bmim][SCN] emerges as the most promising ionic liquid, offering insights into anion selection's role in shaping ionic liquid properties for 1,3-PDO extraction.

Keywords: 1,3-Propanediol, Ionic liquids, Molecular dynamics, COSMO-SAC

1. Introduction

1,3-Propanediol (1,3-PDO), a remarkable three-carbon dialcohol distinguished by its colourless, odourless, and viscous liquid properties, has emerged as a pivotal chemical with widespread utility across diverse sectors (1). These include pharmaceuticals, food production, and the textile industry. The compound's significance lies in its versatile applications as an intermediate compound and within these industries. One of the most useful things about 1,3-PDO is that it is a key monomer in making polypropylene terephthalate (PTT) and polyurethane (PU), which are indispensable components in contemporary material sciences. With projections indicating a market size of US $1442.77 million by 2027 and an annual growth rate of 14.2%, the trajectory of 1,3-PDO's market expansion appears robust (2). While 1,3-PDO production has historically relied on chemical synthesis methods pioneered by Shell and Degussa (now owned by DuPont), contemporary efforts increasingly focus on harnessing biological pathways that capitalize on renewable biomass and microorganisms (3). The drawbacks of chemical methods, such as the production of toxic intermediates, harsh conditions, and expensive catalysts, are what have prompted this shift. Despite this transition, significant challenges persist, particularly in the downstream processing phase, constituting a substantial portion of the total production cost. Additionally, the intricate separation of 1,3-PDO from the fermentation broth is complicated by its high boiling point and strong hydrophilic characteristics (4). Successfully addressing these challenges is pivotal for establishing an economically viable and environmentally sustainable production process.

Efforts to refine the separation of 1,3-PDO from complex fermentation broths have encountered challenges stemming from the use of harsh chemicals and energy-intensive processes. Despite attempts to enhance efficiency with ethanol as a co-solvent, minimal enhancements were observed in the distribution coefficient of 1,3-PDO due to its intrinsic hydrophilic nature (5). While reactive extraction emerged as an innovative avenue by transforming 1,3-PDO into hydrophobic entities via chemical reactions, this approach faced obstacles such as catalyst toxicity, undesired side reactions, and reduced efficiency (6–8), separating 1,3-PDO via ultrafiltration and alcohol crystallization achieved notable impurity removal while acknowledging the energy-intensive nature and membrane pollution associated with electrodialysis (9). Silica gel chromatography demonstrated promise, but limitations in terms of adsorption capacity and resin regeneration persisted on a larger scale (10). While various methods, such as ion exchange, electrodialysis, and two-phase salting-out extraction, have been

investigated for the purification of biologically derived 1,3-PDO, these methods often suffer from issues like high material costs, energy consumption, and wastewater generation (11–14). The two-step salting-out extraction effectively separates 1,3-PDO from butyric acid in fermentation broths, promising high recoveries. However, scalability poses a significant challenge, impacting efficiency and economic feasibility at larger industrial scales (15). Enzymatic 1,3-PDO separation involves esterification and lipase-directed hydrolysis. Complex fermentation broth components cause side reactions, catalyst toxicity, and reduced efficiency. Diverse poly-alcohol analogues showed efficient separation with 96% recovery (16). Additionally, preparative chromatography, fixed-bed resin adsorption, and reactive extraction entail the use of substantial quantities of organic solvents or hazardous reactants, thereby rendering them unsuitable for large-scale industrial applications (17–19). The complex mixture of extractants, precise molar ratios, and high operating temperatures (80 °C) in the multi-alcohol synergistic extraction process for 1,3-PDO recovery present optimization challenges. Additionally, the process's extended duration and reliance on specific extractants might hinder scalability and cost-effectiveness (20). The need for a comprehensive evaluation, encompassing final purity, yield, waste handling, and cost considerations, is critical as these processes move from the lab to industry. Consequently, developing a holistic and efficient downstream process that overcomes these challenges remains a pivotal concern, and ionic liquids present a promising avenue for addressing these limitations.

The limitations of traditional methods for 1,3-PDO separation are the driving force behind our study. In response to these challenges, we focus on exploring alternative, more sustainable, and efficient separation methodologies. We are particularly drawn to investigating the potential of ionic liquids (ILs) as a viable solution. At the core of our investigation is the challenge of identifying an optimal solvent alternative for efficient 1,3-propanediol (1,3-PDO) separation. This is intricately linked to pursuing sustainable solutions in chemical processes. Ionic liquids (ILs) emerge as a promising class of compounds to address this, celebrated as "green solvents" with minimal environmental impact. Non-volatile ILs are pragmatic substitutes for both hazardous and conventionally volatile solvents, diminishing emissions and fostering cost-effective processes. Within this context, ILs offer the transformative potential for 1,3-PDO separation. Their unique attributes, tunable chemical structures, and physicochemical properties enable selective compound extraction (21). Certain ILs hold promise for efficient isolation from

fermentation broths. Several studies have explored the capacity of imidazolium-based ILs for separating components from mixtures (22–32). Alkyl-imidazolium (Im_4)-based ILs with the $[NTF2]^-$ anion demonstrated diverse hydrophobicity levels, and this hydrophobicity correlated linearly with butanol distribution, with 1-butanol distribution coefficients ranging from 1.10 to 1.90 in aqueous solutions, affirming their proficiency in butanol extraction (33–35). This finding reinforced the established correlation between the length of alkyl chains and hydrophobicity in ILs, specifically those involved in forming aqueous biphasic systems (ABS). As highlighted in prior research, various ionic liquids were shown to form effective ABS system (phosphate/$Im_{4,1}$-CF_3SO_3/water) for 1,3-propanediol extraction. Distribution coefficients ranging from 1.5 to 27.7 indicated a preference for accumulation of 1,3-PDO in the ionic liquid-rich phase. This phenomenon was influenced by the polarity and hydrogen-bond accepting strength of the anion or cation, with the anion exerting a more significant influence than the cation (36). Dicyanamide $[DCA]^-$ based ILs demonstrated effective extraction of isopropanol (IPA) from di-isopropyl ether (DIPE), isopropyl alcohol (IPA) and IL mixtures (37). Another investigation focused on ILs with ethyl alkyl chains, revealing that $[SCN]^-$ anion based ILs displayed enhanced selectivity for alcohol extraction compared to $[TFO]^-$ based ILs (38). Additionally, research examined imidazolium-based ILs with varying alkyl chain lengths and the $[NTF2]^-$ for separating water and propanol mixtures. Findings indicated that $[NTF2]^-$ based ILs exhibited higher extraction efficiency, with a correlation between alkyl chain length and extraction ability. Longer alkyl chains were associated with increased ionic liquid (IL) viscosity. Considering these insights, a study explored butyl imidazolium-based ILs containing $[SCN]^-$, $[DCA]^-$, and $[NTF2]^-$ for targeted separations (39,40). The miscibility of ILs was demonstrated to be anion-specific, and for diols, the observed sequence was as follows: $[BF_4]^- > [NTF2]^- > [PF_6]^-$ (41).

Although many different ILs can be manufactured for use in many different contexts, choosing among them sometimes requires lengthy, challenging, and costly experimental techniques. Classical MD simulation decodes experimentally elusive processes, navigating extremes in conditions and time scales. Economical and nanosecond-precise, it unveils atomic-level phenomena via trajectory analysis, exposing changes unseen by conventional instruments. The answers to fundamental molecular issues and new solvents can be found by molecular dynamics (MD) simulations. Researchers have used quantum chemistry and MD simulations to learn more about the hydrogen bonding in alcohols by examining the correlation between microstructure and

macroperformance (42). To better understand the extraction process and to determine the optimal IL, MD modeling was used to explore the local structures of three distinct imidazole IL-MeOH-NHA (methanol-hexane) systems. MeOH and NHA extraction employing ILs, diffusion, and structural features determined from MD phase equilibrium data showed a discrepancy of less than 8% from experimental data (43). MD simulations of the deep eutectic solvent (DES), water, and nitenpyram ternary system showed promising results that matched experimental literature (44). Several aqueous component extraction methods have been documented using MD simulation (45–47).

Lin and Sandler introduced the COSMO-SAC (COSMO-Segment Activity Coefficient) model as a novel activity coefficient model, building upon the COSMO-RS (48) and COSMO models, and further proposing a fragment coefficient activity model (COSMO-SAC) (49). The COSMO-SAC model predicts essential thermodynamic properties like activity coefficients and phase balances for pure fluids or mixtures without experimental data, using quantum chemical calculations (50,51). At its core, σ-profiles, derived through quantum calculations, describe molecular interactions with solvents (52). They reveal intricate donor-acceptor relationships, particularly in hydrogen bonding, providing a fundamental basis for predicting thermodynamic properties accurately (53). This knowledge improves our understanding of molecular behavior in solvents and enhances predictions of partition coefficients, activity coefficients, and phase balances in various chemical systems. Shah et al. (54) applied the COSMO-SAC model to predict liquid-liquid equilibria (LLE) in biofuel production and bio-alcohol extraction using ionic liquids. The model exhibited reasonable performance for systems involving methyl oleate, methanol, glycerol, and methyl laurate, ethanol, glycerol. Xu et al. (55) utilized the COSMO-SAC model to screen ionic liquids for coal tar oil fraction extraction, which contributed to the concept of separating coal tar fractions.

Meanwhile, Bharti et al. (56) employed the COSMO-SAC model for phase equilibria predictions. Their results showed that the model performed well for organic solvent-based systems with a rmsd below 8.00%, while it exhibited less accuracy with a rmsd between 16.81 and 18.53% for ionic liquid-based systems. This suggests that the COSMO-SAC model is more reliable in predicting systems without ionic liquids.

In this research, our primary approach involved the integration MD simulations and quantum chemical calculations (COSMO-SAC). By using this integrated approach, we aimed to elucidate

the intricate interactions and mechanisms governing the separation process, ultimately providing a thorough understanding of how anions within ionic liquids influence the efficiency of 1,3-PDO separation. Molecular Dynamics simulations were employed to investigate the interactions and performance of four distinct ionic liquids ([Bmim][NTF2], [Bmim][NPF2], [Bmim][SCN], and [Bmim][TFO]) as potential extraction agents for 1,3-propanediol (1,3-PDO). The fundamental objective of this computational study is to learn about the molecular-level behaviors and interactions of these molecules without resorting to actual experiments. We investigated the structural and dynamic interplay between imidazolium-based ILs and 1,3-propanediol (1,3-PDO) using molecular dynamics simulations. Subsequently, σ-profiles were generated via the COSMO-SAC model, allowing for the examination of hydrogen bond donor and acceptor relationships to verify their impact on the system. Our research aimed better to understand the complex molecular behaviors inside this system, ultimately leading to improved separation techniques and more environmentally friendly chemical engineering solutions. We evaluated the effectiveness of these ionic liquids in establishing interactions with 1,3-PDO and identified the most favorable candidate for potential applications. The key elements of our analysis within our investigation are listed in Table 1.

2. Methodology

2.1. Force field:

The OPLS-AA (optimized Potentials for Liquid Simulations-All Atom) force field has been widely utilized to simulate imidazolium-based ionic liquids, including those containing 1,3-propanediol (1,3-PDO). The OPLS-AA force field calculates the total energy of a molecular system by summing individual intra- and intermolecular energy terms (57). The harmonic potential was used to describe bond stretching and angle bending, while the OPLS force field was employed to model dihedral torsions. The total energy in the OPLS-AA force field is given by equation 5.

$$\mathbf{E_{Bonds}} = \sum_{\mathbf{bonds}} \mathbf{K_{b,i}} \left(\mathbf{r_i} - \mathbf{r_{o,i}}\right)^2 \quad \textbf{(1)}$$

$$\mathbf{E_{Angles}} = \sum_{\mathbf{Angles}} \mathbf{K_{\theta,i}} \left(\boldsymbol{\theta}_\mathbf{i} - \boldsymbol{\theta}_\mathbf{o,i}\right)^2 \quad \textbf{(2)}$$

$$\mathbf{E_{Dihedrals}} = \sum_{\mathbf{Dihedrals}} [\frac{\mathbf{1}}{\mathbf{2}}\mathbf{V_{1,i}}(\mathbf{1}+\mathbf{cos\phi}) + \frac{\mathbf{1}}{\mathbf{2}}\mathbf{V_{2,i}}(\mathbf{1}-\mathbf{cos\,2\phi}) + \frac{\mathbf{1}}{\mathbf{2}}\boldsymbol{V_{3,i}}(\mathbf{1}-\mathbf{cos\,3\phi}) + \frac{\mathbf{1}}{\mathbf{2}}\boldsymbol{V_{4,i}}(\mathbf{1}-\mathbf{cos\,4\phi}) \quad \mathbf{(3)}$$

$$\mathbf{E_{Nonbonded}} = \sum_{\mathbf{i}}\sum_{\mathbf{j>1}} \{\frac{\mathbf{q_i q_j e^2}}{\mathbf{r_{ij}}} + \mathbf{4}\epsilon_{\mathbf{ij}}[\left(\frac{\boldsymbol{\sigma}_{\mathbf{ij}}}{\mathbf{r_{ij}}}\right)^{\mathbf{12}} - \left(\frac{\boldsymbol{\sigma}_{\mathbf{ij}}}{\mathbf{r_{ij}}}\right)^{\mathbf{6}}]\} \quad \mathbf{(4)}$$

$$\mathbf{E_{Total}} = \mathbf{E_{Bonds}} + \mathbf{E_{Angles}} + \mathbf{E_{Dihedrals}} + \mathbf{E_{Nonbonded}} \quad \mathbf{(5)}$$

The equation (4) accounts for electrostatic and nonbonded interactions between atoms. The electrostatic energy is calculated using Coulomb's law, considering the partial atomic charges ($q_i q_j$), interatomic separation (r), and the dielectric permittivity constant for vacuum (ϵ_0) whereas nonbonded interactions are calculated by the 12-6 Lennard-Jones potential and depends on the interatomic separation (r), energy well depth (ε), and interatomic separation at zero potential (σ).

In the case of imidazolium-based ionic liquids, the OPLS-AA force field parameters has been taken from Doherty et al. (58) which is based on the OPLS frameworks with some minor modifications. This refined force field has been shown to accurately capture the properties of imidazolium-based ionic liquids. For 1,3-PDO molecule, the force field parameters were assigned using the Ligpargen web server using 1.14*CM1A charge models (59), a tool specifically designed for parameterizing small organic molecules within the OPLS-AA force field framework (60,61). The force field parameters for the Tip3P (transferable intermolecular potential 3P) water model were selected to ensure the correct density (62), with no consideration given to charge scaling.

2.2. Simulation details:

A total of 350 ion pairs of ionic liquid (ILs) and 350 molecules of 1,3-PDO were packed using the PACKMOL software to create the initial system configuration (63). Figure 1 shows the chemical structures of the components along with the atom types used in this work. The simulation was performed using LAMMPS software (LAMMPS-64bit-8Feb2023.exe) (64). The simulation was conducted by employing the "full" atom style in a three-dimensional (3D) space with periodic boundary conditions in all dimensions. The intermolecular interactions were

modelled using the Lennard-Jones (LJ) potential with a cutoff of 13.0 Å, incorporating tail correction and geometric mixing rules. The equations of motion were integrated numerically using the velocity-Verlet algorithm with a time step of 1.0 fs. The LINCS algorithm was used to constrain covalent bonds to hydrogen atoms, maintaining their stability throughout the simulation (65). For long-range electrostatic interactions, the PPPM (Particle-Particle Particle-Mesh) method was employed (66). To control the temperature and pressure during the NPT simulation, the Nose-Hoover thermostat (67,68) and Parinello-Rahman barostat (69) were employed. The Nose-Hoover thermostat rescaled the velocities of the atoms to maintain a constant temperature, while the barostat adjusted the simulation box volume to keep the pressure constant at 1 atm. Prior to the simulation, the system was minimised using the steepest descent algorithm to optimise the initial configuration. Initial velocities were assigned to all atoms according to a Gaussian distribution at the specified temperature to ensure a realistic starting state for the simulation. The simulation process involved successive NPT ensemble simulations. During the subsequent simulation, the temperature is systematically raised from 298 K to 600 K over the course of a 2 ns run. This gradual increase allows the system to equilibrate at the elevated temperature while keeping the pressure constant. Initially, the system was equilibrated at 600 K for a duration of 2 ns. This was followed by an NPT simulation where the temperature was gradually reduced from 600 K to 298 K over a period of 2 ns. This temperature annealing process ensures proper mixing of the ionic liquid and is essential for achieving equilibrium in viscous systems.

Following the equilibration process, a production run was conducted for 12 ns in the NPT ensemble at a temperature of 298 K and a pressure of 1 atm for the estimation of density. To ensure comprehensive analysis, the simulation was extended to capture sufficient system sampling. The radial distribution functions (RDF) and spatial distribution functions (SDF) were extensively examined to gain insights into molecules spatial arrangement and distribution within the system. The analysis involves simulation over a period of 30 ns, ensuring a comprehensive exploration of particle dynamics. The TRAVIS program was used for SDF analysis (70). The correct isovalue was chosen so that the SDF could be viewed in all three dimensions. The number of hydrogen bonds was analysed using VMD to provide insights into the nature and strength of interactions between the ionic liquids and 1,3-PDO, offering valuable information on the stability and potential for efficient interactions (71).

In the context of 1,3-PDO extraction, molecular dynamics were done for water-ILs-1,3-PDO ternary systems to simulate the extraction process as closely as possible to experimental conditions. Due to computational constraints, replicating the exact number of experimental molecules wasn't feasible. Consequently, our simulated system comprises a 1:1 mass ratio between ILs and aqueous mixture, with an initial presence of 20% 1,3-PDO molecules in the aqueous phase. The TiP3P water model was employed for this simulation. Table 2 provides a summary of the number of ion pairs of ionic liquids (ILs), 1,3-propanediol (1,3-PDO), and water molecules utilized in our study. The simulation box dimensions measure 170 x 70 x 70 Å. Specifically, the ILs occupy the region from 0 to 70 Å, while the mixture of 1,3-PDO and water molecules is confined within the box spanning from 70 to 170 Å. The construction of this solvation box was meticulously executed using the PACKMOL software. The SHAKE algorithm was applied in the TiP3P water model to maintain bond lengths during the simulation (72). The system, under periodic boundary conditions (PBC), commenced its equilibration process at an initial temperature of 5 K. Subsequently, the water box was equilibrated at temperatures of 10 K, 100 K, 150 K, 200 K, and 300 K before reaching a final equilibration at 400 K. A timestep of 0.5 fs was employed, and the system was run for 1 ns at each temperature. Following the successful equilibration process, the system was gradually cooled down to a target temperature of 298 K. At this temperature, a production run lasting 30 ns was conducted under the NPT ensemble conditions (73).

2.3. Quantum chemical predictions using COSMO-SAC:

The quantum chemical-based conductor like screening model-segment activity coefficient (COSMO-SAC) was used to predict the infinite dilution activity coefficient of 1,3-PDO in ILs (74–77). The computational procedure for the COSMO-SAC calculations involved several key steps which are discussed below. The molecular structures of the molecules of interest, such as 1,3-PDO, [BMIM][SCN], [BMIM][TFO], [BMIM][NTF2], and [BMIM][NPF2], were initially drawn using the Avogadro (version 1.2.0), an open-source molecular builder and visualization tool (78). To optimize these molecular structures, the Gaussian16 computational package was employed (79). The optimization utilized the B3LYP (Becke 3-parameter hybrid functional combined with the Lee-Yang-Parr correlation) theory and the 6-311++g (d, p) basis set (80–82). Additionally, frequency calculations were carried out to ensure that the optimized structures

corresponded to energy minima. Upon satisfactory geometry optimization, the COSMO files were generated for each molecule using Gaussian16. This was accomplished by applying the BVP86/TZVP/DGA1 level of theory and basis set (83). The "scrf=COSMORS" keyword was integrated into the calculations to indicate the use of the COSMO solvation model. The generated COSMO files were then utilized as inputs for the COSMOSAC software (84). COSMOSAC is open-source software that implements COSMO-SAC models using a combination of C++ and Python. This software took the provided COSMO files as input and computed sigma profiles, which characterize the electrostatic interactions between solute molecules and solvent environments. Subsequently, the sigma profiles obtained from the COSMOSAC calculations were once again employed as input for the COSMOSAC software. Through this step, the software facilitated the calculation of the infinite dilution activity coefficient of 1,3-propanediol in the ionic liquids under investigation.

3. Results and Discussions:

3.1. Molecular dynamics simulation:

3.1.1. Experimental validation:

Before studying the binary and ternary systems, the density of pure components involved in the present work was estimated to validate the force field parameters and then compared with the reported experimental and simulation data (85–89). Table 3 presents the estimated density values for the various systems, while Figure S6 provides a visual representation of the density profiles over 12ns simulation. The simulated densities of the pure systems were compared to experimental values using charge scaling factors of ±0.8 and ±1.0. The average absolute relative deviation (AARD) analysis indicated that the ±0.8 scaling factor produced a low relative deviation, with an AARD of 0.51%. Conversely, the ±1.0 scaling factor resulted in a slightly higher relative deviation, with an AARD of 3.05%. These results highlight the superior accuracy of the ±0.8 scaling factor in estimating the densities compared to the ±1.0 scaling factor for the components involved in the present study. The absolute relative deviation for 1,3-PDO is less than 2% while for pure ILs the variation is less than 0.3% for ±0.8 charge scaling factor. Further, the RDF and SDF of pure ILs were evaluated, as shown in Figure S7-13.

3.1.2. Structural analysis:

In the analysis of the system structure, the RDF and SDF were examined to study the interactions between the ILs and 1,3-PDO. These distribution functions provided insights into the spatial arrangement and density distribution of molecules, revealing the nature and strength of interactions between ILs and 1,3-PDO. The RDF is a statistical tool used to analyze the spatial arrangement of 1,3-PDO particles in a system of ILs-1,3-PDO. Equation 6 describes this function.

$$\mathbf{g(r) = \frac{\langle \rho(r) \rangle}{\rho}} \quad \textbf{(6)}$$

Where, ρ(r) is the number density of particles at distance "r", and ρ is the overall number density of particles in the system. It quantifies the probability of finding a particle at a certain distance from a reference particle. This approach enables us to gain insights into particle distribution patterns and interactions, contributing to a deeper understanding of the behavior of the system under study. The coordination number (CN) is calculated by integrating the radial distribution function (g(r)) up to the position of the first solvation shell, which is identified by the first local minimum in the g(r) curve.

$$\mathbf{CN = 4\pi\rho \int_0^{Rmin} r^2 g(r) dr} \quad \textbf{(7)}$$

Where, $4\pi r^2 dr$ is Volume element in a spherical shell, $\int_0^{Rmin}$, Integral over the range of distances from 0 to R_{min}, r^2 is radial distance squared, g(r) is radial distribution function, dr is differential element of distance (90). This method provides a quantitative measure of the particles arrangement and interactions in the system. These RDF analyses showed how molecules were spread out in space and how often and how close certain atoms or groups in the ILs and 1,3-PDO interacted with each other. The outcomes of these analyses, which considered the center of mass of the cations and anions, and the position of carbon (Cc) in 1,3-PDO molecules as reference points to calculate distances, are visually represented in Figure 2. This figure showcases the molecular dynamic simulations involving the ILs and 1,3-PDO at a temperature of 298 K. Furthermore, the data is shown in Table 4.

The analysis of interactions in [Bmim][NPF2] between the anion ($[NPF2]^-$) and 1,3-PDO, as well as the cation ($[Bmim]^+$) and 1,3-PDO, unveiled intriguing insights as shown in Figure 2a. RDF analysis identified a peak at 5.60 Å, indicating the most probable distance between the [NPF2] anion and 1,3-PDO. With a peak value of 1.50 indicating a moderate likelihood of finding 1,3-

PDO molecules around the [NPF2] anion, the coordination number of 2.80 suggests the presence of approximately 2.80 1,3-PDO molecules in the first solvation shell. In contrast, ($[Bmim]^+$) displayed a lower coordination number and a smaller first solvation shell, suggesting a weaker interaction with 1,3-PDO. In the MD simulation of [Bmim][NTF2] as depicted in Figure 2b, the analysis of interactions with 1,3-PDO revealed a peak at 6.57 Å for the [NTF2]-1,3-PDO interaction. The coordination number of 3.28 suggests the presence of approximately 3.28 1,3-PDO molecules within the first solvation shell. In the $[Bmim]^+$-1,3-PDO interaction, the RDF peak at 5.00 Å, with a peak value of 1.56, indicated the likelihood of finding 1,3-PDO molecules around the [Bmim] cation. A coordination number of 2.78 suggest, 2.78 1,3-PDO molecules in the first solvation shell. The anion ($[NTF2]^-$) and cation ($[Bmim]^+$) of [Bmim][NTF2] demonstrate higher coordination numbers and larger first solvation shells than [Bmim][NPF2], suggesting stronger and more favorable interactions with 1,3-PDO.

Figure 2c, shows that the interaction between [Bmim][SCN] and 1,3-PDO occurs on two different coordination shells. Due to the loose packing of particles in liquids, multiple such coordination layers are possible (91). The distance between the $[SCN]^-$ and the 1,3-PDO was calculated using the RDF and found to be around 7.08 Å. In addition, the coordination number was around 6.12. Similarly, we observed that the most likely distance between the $[Bmim]^+$ and 1,3-PDO molecules was around 5.26 Å, with a peak value of 1.6 indicating the likelihood of finding 1,3-PDO molecules near the $[Bmim]^+$. Coordination number was about 7.00, so there were roughly seven 1,3-PDO molecules within a few nanometers of each $[Bmim]^+$. Figure 2d illustrates the interactions between the anion ($[TFO]^-$) of the IL [Bmim][TFO] and 1,3-PDO, as well as between the cation ($[Bmim]^+$) of the IL and 1,3-PDO. The RDF analysis revealed that the RDF peak for the $[TFO]^-$-1,3-PDO interaction occurs at a distance of 5.40 Å, with a peak value of 1.60 and a coordination number of 3.56. For the $[Bmim]^+$-1,3-PDO interaction, the RDF peak occurs at a distance of 5.78 Å, with a higher peak value of 2.08 and coordination number of 3.33. Both the anion ($[SCN]^-$) and cation ($[Bmim]^+$) of [Bmim][SCN] exhibit notably higher coordination numbers than other ILs, indicating stronger interactions with a greater presence of 1,3-PDO molecules. [Bmim][SCN] stands out with a coordination number of 6.12 for $[SCN]^-$ and 7.0 for $[Bmim]^+$, highlighting a stronger interaction and a larger concentration of 1,3-PDO molecules. A higher coordination number suggests that more solvent molecules are surrounding the ion, indicating a stronger interaction, contributing to a stable and well-solvated system.

The spatial distribution function analyses, SDFs, were carried out to obtain detailed information on the molecular structure of 1,3-PDO and ILs at 298 K. The SDFs indicated the average density distribution of the 1,3-PDO around cation and anion as a reference in the ILs, as shown in Figure 3a-d. Our investigation involved analyzing the SDF of 1,3-PDO around the ILs [Bmim][NPF2], [Bmim][NTF2], [Bmim][SCN], and [Bmim][TFO], which yielded significant insights into their solvation behavior. The iso-value for anions is set at 4, whereas for cations, it is set at 3. Among the ILs studied, [Bmim][SCN] demonstrated the highest distribution of 1,3-PDO, exhibiting a strong solvation preference around both the cation $[Bmim]^+$ and the anion $[SCN]^-$. Additionally, [Bmim][TFO] displayed the second highest distribution of 1,3-PDO, followed by [Bmim][NTF2] and further, [Bmim][NPF2], which exhibited the least distribution.

The observed variations in 1,3-PDO distribution around different ILs underscore the significant influence of the anions on the solvation behavior. The $[SCN]^-$ in [Bmim][SCN] seems to create a favorable solvation environment, leading to higher 1,3-PDO distribution around both the cation and anion. Similarly, the $[TFO]^-$ in [Bmim][TFO] appears to play a crucial role in enhancing the solvation preference around the cation $[Bmim]^+$. In contrast, the $[NPF2]^-$ in [Bmim][NPF2] contributes to a less favorable solvation environment, resulting in the lowest 1,3-PDO distribution among the ILs studied. These findings highlight the pivotal role of anions in influencing the solvation behavior of 1,3-PDO and offer valuable insights into the interplay between cations and anions in ILs. Understanding these interactions is crucial for rationalizing the selection and design of ILs for diverse applications, where solvation plays a pivotal role. These findings suggest that [Bmim][SCN] exhibits the strongest interactions and preferences for 1,3-PDO, highlighting its potential as an efficient solvent for 1,3-PDO-related applications.

In addition to studying the distribution of 1,3-PDO around different ILs, we also investigated the distribution of ILs around 1,3-PDO as shown in Figure S14a-d. The isovalue for the anions and cations was set at 2.7 times the reference density. Interestingly, we found that the distribution of ILs around 1,3-PDO exhibited notable variations depending on the specific IL considered. The distribution of ILs around 1,3-PDO provides valuable information about the mutual interactions between the IL and 1,3-PDO. Among the ILs studied, [Bmim][SCN] showed a relatively high distribution around 1,3-PDO, indicating a stronger preference for solvating 1,3-PDO molecules. This finding suggests favorable interactions between [Bmim][SCN] and 1,3-PDO, leading to a higher density of IL in proximity to 1,3-PDO. Similarly, [Bmim][TFO] also displayed a

significant distribution around 1,3-PDO, indicating a favorable solvation behavior. On the other hand, [Bmim][NPF2] exhibited a lower distribution around 1,3-PDO, suggesting weaker solvation interactions. The differences in the distribution of ILs around 1,3-PDO reveal varying affinities and interactions between ILs and the 1,3-PDO, underscoring the importance of the IL's specific chemical structure in influencing mutual solvation.

Overall, studying how ILs are distributed around 1,3-PDO adds to our analysis and helps us learn more about how ILs and 1,3-PDO interact when they come into contact with each other. The mutual solvation behavior between 1,3-PDO and the studied ILs varied significantly. [Bmim][SCN] exhibited the strongest density around 1,3-PDO, followed by [Bmim][TFO], [Bmim][NTF2], and [Bmim][NPF2], indicating distinct affinities and interactions.

3.1.3. Comparative SDF and RDF analysis of ionic liquid interactions with 1,3-propanediol:

The meticulous exploration of the interactions between 1,3-PDO and four distinct ILs - [Bmim][NPF2], [Bmim][NTF2], [Bmim][SCN], and [Bmim][TFO], through both RDF and SDF analyses unveils essential insights into the nature, strength, and distinctiveness of these interactions, facilitating the identification of the IL that establishes the most favorable interactions for potential applications.

The SDF analysis of [Bmim][NPF2] as shown in Figure 4a-d, reveals potential interactions, with intensified density around the anion's oxygen atom and concentrated density around a hydrogen atom of 1,3-PDO's hydroxyl group, suggesting hydrogen bonding. The distribution of [Bmim]+ around the oxygen atom of 1,3-PDO's hydroxyl group provides further evidence of potential hydrogen bonding interactions. In Figure 4e, RDF analysis highlights significant peaks between $[Bmim]^+$ hydrogen and 1,3-PDO oxygen (CN: 0.35) and $[NPF2]^-$ nitrogen and 1,3-PDO hydrogen (CN: 0.76), indicating potential hydrogen bonding. Additional peaks involving [N] of cation & [O] of 1,3-PDO and [H] of cation & [O] of 1,3-PDO affirm interaction stability. The combined insights from SDF and RDF analyses strongly suggest the presence of hydrogen bonding interactions between [Bmim][NPF2] and 1,3-PDO.

Moving to [Bmim][NTF2] as depicted in Figure S15a-d, the SDF analysis echoes the patterns observed in [Bmim][NPF2]. Akin to the previous IL, the density distribution around the anion's oxygen atom indicates attractive forces that may involve hydrogen bonding. The cation's presence around the oxygen atom of 1,3-PDO and the anion's presence around 1,3-PDO's

hydroxyl group hydrogen atom suggest potential hydrogen bonding interactions, mirroring the observations in [Bmim][NPF2]. The denser distribution of 1,3-PDO around both the cation and anion in [Bmim][NTF2], in comparison to [Bmim][NPF2], points to more favorable interactions. Figure S15e depicts the RDF analysis, affirms relatively stable interactions between specific atom pairs, although the absence of sharp peaks implies less specificity.

In [Bmim][SCN], SDF analysis as illustrated in Figure 5a-d, reveals widespread 1,3-PDO density, showcasing diverse interactions beyond the 1,3-PDO's hydroxyl group hydrogen, encompassing various hydrogen atoms. $[Bmim]^+$ cations are distributed along the alkyl chain, and their significant presence around 1,3-PDO's oxygen suggests potential hydrogen bonding. As shown in Figure 5e, the RDF analysis emphasizes robust interactions, with peaks between $[SCN]^-$ nitrogen, sulfur, and carbon atoms, and 1,3-PDO's hydrogen atoms indicating strong hydrogen bonding. These observations, combined with the $[Bmim]^+$ distribution and the diverse interaction landscape, highlight [Bmim][SCN]'s unique potential for forming versatile and stable interactions with 1,3-PDO. Similarly, a peak with a height of 6, CN of 0.51, and a first solvation shell at 2.78 Å between $[SCN]^-$ sulfur and 1,3-PDO's hydroxyl group hydrogen suggests a stable interaction. Another peak, with a height of 4, CN of 0.92, and a first solvation shell at 4.40 Å between $[SCN]^-$ carbon and 1,3-PDO's hydroxyl group hydrogen, points to a significant interaction. Examining the cationic portion, a peak with a height of 1.80, CN of 1.80, and a first solvation shell at 6 Å between [Bmim] cation nitrogen and 1,3-PDO's oxygen indicates a stable interaction, likely involving hydrogen bonding between the nitrogen atom of the cation and the oxygen atom of 1,3-PDO. Compared to other ILs, [Bmim][SCN] stands out for its unique features, showcasing profound peaks at various atom pairs involving $[SCN]^-$ and 1,3-PDO, highlighting versatile hydrogen bonding capabilities. The broader range of interactions involving $[SCN]^-$ anion and various hydrogen atoms of 1,3-PDO, along with the presence of [Bmim] cations along the alkyl chain, illustrates a more dispersed and complex interaction landscape in this system. Figure 6a-d provides a clear illustration of the interaction dynamics occurring within the [Bmim][TFO] system, the SDF analysis emphasizes the density of 1,3-PDO around the oxygen atom of the $[TFO]^-$ anion, indicating strong attraction between these two components. Furthermore, the density distribution of 1,3-PDO around various hydrogen atoms of the [Bmim] cation, with a concentration around the hydrogen atom on the [Bmim] ring, underscores the potential for hydrogen bonding interactions. The RDF analysis for [Bmim][TFO] reveals distinct

interaction patterns compared to the other studied ILs. Peaks between specific atoms of the [TFO] anion and the hydrogen atoms of 1,3-PDO exhibit notable characteristics (Figure 6e). The oxygen and sulfur atoms of the $[TFO]^-$ show strong RDF peaks with heights of 6.00, suggesting robust hydrogen bonding interactions. This signifies the presence of well-defined hydrogen bonds that may contribute to a stable interaction. Conversely, the fluorine atom of the $[TFO]^-$ and the hydrogen atom of 1,3-PDO exhibit broader and smaller RDF peaks, possibly indicating a broader range of interactions or a more transient hydrogen bonding network. Additionally, in the cation portion, the RDF peaks involving the hydrogen atom on the [Bmim] ring and the oxygen atom of 1,3-PDO show a smaller peak height at 1.80, albeit with a moderate CN of 0.51. On the other hand, the RDF peak between the nitrogen atom at the center of the [Bmim] ring and the oxygen atom of 1,3-PDO displays a peak height of 1.80, with a CN of 1.75.

In summary, a comparative analysis of RDF and SDF data reveals intricate interactions between 1,3-PDO and the selected ionic liquids (ILs). [Bmim][TFO] and [Bmim][SCN] exhibit stronger RDF anion peaks than [Bmim][NPF2] and [Bmim][NTF2], emphasizing the significant role of their anions ($[TFO]^-$ and $[SCN]^-$) in influencing interactions with 1,3-PDO. The intensified RDF anion peaks suggest more significant hydrogen bonding interactions between the anions and 1,3-PDO. Conversely, weaker cation peaks hint at relatively less prominent cationic interactions. This dynamic interplay underscores the delicate equilibrium between interaction strength and stability, with anions showcasing potent yet potentially less stable interactions, while cations engage in more stable but comparatively weaker interactions. The correlation function between nitrogen in thiocyanate and hydrogen in propanediol shows a narrow initial peak that drops virtually to zero for mixes, as seen in Figure 5e. Due to the persistent formation of hydrogen bonds between the N group in [Bmim][SCN] and 1,3-PDO, the number of closest hydrogen neighbors surrounding a nitrogen atom exhibits a highly distinct step-wise pattern, with a stable plateau at a value of 0.63 in pure liquid systems. As seen in Figure 6e, the sulphur of trifluoromethanesulfonate and hydrogen of 1,3-PDO exhibit a similar pattern for the first peak, confirming its role in hydrogen bonding (92).

This study accentuates the dynamic nature of hydrogen bonding within IL-1,3-PDO interactions. Both [Bmim][TFO] and [Bmim][SCN] stand out with stronger RDF anion peaks, underscoring their substantial influence on these interactions (93). The versatile hydrogen bonding dynamics between anions and 1,3-PDO, coupled with more stable yet comparatively weaker cationic

interactions, deepens our understanding of the intricate balance in IL-1,3-PDO systems, contributing to their potential applications.

3.1.4. Hydrogen bond analysis:

In our research study, we investigated the intriguing hydrogen bonding interactions between 1,3-PDO and four different ILs: [Bmim][NPF2], [Bmim][NTF2], [Bmim][SCN], and [Bmim][TFO]. These interactions play a pivotal role in understanding the behavior and properties of these mixtures, especially considering the molar ratio of 1:1 for ILs and 1,3-PDO. Calculating the number of hydrogen bonds between the cation and anion of the ILs with 1,3-PDO serves as a quantitative validation of the interactions observed through RDF and SDF analyses. It acts as a bridge between qualitative observations and quantitative data, helping to eliminate uncertainties in interpretation. By counting hydrogen bonds, we can conclusively determine which IL shows more favorable interactions with 1,3-PDO and provides a clearer picture of their potential applications. Hydrogen bond estimates are consistent with previously described geometric criteria (94,95). Insights from Figures 4-6 of the RDF were used to determine a cutoff donor-acceptor distance of 3.5 Å and an angle cutoff of 30°, as guided by the findings presented by Pethes et al. (96) .

The bar graph in Figure 7 showcases the average number of hydrogen bonds formed between ILs and 1,3-PDO molecules, represented by the orange bars, as well as the number of hydrogen bonds formed between the anions of ILs and 1,3-PDO per 1,3-PDO molecule, represented by the green bars. The data highlights the role of both ILs and their anions in influencing the strength and nature of hydrogen bonding interactions with 1,3-PDO, providing insights into the behavior and properties of these mixtures for potential applications in green chemistry and sustainable technologies. Hydrogen bonding occurs when the $[OH]^-$ groups in 1,3-PDO form connections with charged species present in the ionic liquids, such as anions or cations. The total number of hydrogen bonds indicated the overall strength of interactions between the ionic liquids and 1,3-PDO, while the number of hydrogen bonds per 1,3-PDO molecule with the anions showcased the specific contributions of the anions to these interactions. [Bmim][NPF2] and [Bmim][NTF2], with their respective non-coordinating anions, displayed slightly lower total hydrogen bond numbers (0.654 and 0.952, respectively). Both [Bmim][NPF2] and [Bmim][NTF2] have non-coordinating anions, $[NPF2]^-$, and $[NTF2]^-$, respectively. The non-coordinating nature of these

anions means they may not form strong hydrogen bonds with 1,3-PDO. The number of hydrogen bonds between the anions of these ionic liquids and 1,3-PDO per 1,3-PDO molecule is relatively lower (0.604 for [Bmim][NPF2] and 0.872 for [Bmim][NTF2]). The weaker hydrogen bonding interaction contributes to a less pronounced influence on the behavior and properties of the mixtures compared to other ionic liquids. Notably, [Bmim][SCN] exhibited the highest total number of hydrogen bonds (1.639) with 1,3-PDO, indicating a relatively stronger interaction. [Bmim][SCN] contains the anion $[SCN]^-$, which has a sulfur atom capable of forming hydrogen bonds with the $[OH]^-$ groups of 1,3-PDO(97). This unique hydrogen bonding interaction leads to a higher number of hydrogen bonds between the anion and 1,3-PDO per 1,3-PDO molecule (1.548). The presence of this stronger hydrogen bonding interaction significantly influences the behavior and properties of the mixtures. Similarly, [Bmim][TFO] showcased a considerable total number of hydrogen bonds (1.331) with 1,3-PDO. The $[TFO]^-$ anion, a trifluoromethanesulfonate ion, contains fluorine atoms capable of forming hydrogen bonds with the $[OH]^-$ groups of 1,3-PDO. This results in a considerable number of hydrogen bonds between the anion and 1,3-PDO per 1,3-PDO molecule (1.309). These findings highlight the remarkable role of anions in mediating hydrogen bond formation between the ionic liquids and 1,3-PDO. The specific interactions between the anions and 1,3-PDO are key determinants in shaping the overall behavior and properties of these mixtures, rendering them highly versatile and potentially suitable for various applications. The presence of different anions in ionic liquids affects the interaction with 1,3-PDO in various ways. Non-coordinating anions like $[NPF2]^-$ and $[NTF2]^-$ result in weaker hydrogen bonding interactions. On the other hand, anions with electronegative atoms like $[SCN]^-$ and $[TFO]^-$ form stronger hydrogen bonds with the $[OH]^-$ groups of 1,3-PDO, leading to enhanced stability and solubility of the mixtures. The selection of the anion significantly influences its impact associated with the anion's capacity to engage in hydrogen bonding (98). Understanding these anion-driven interactions is crucial for tailoring the performance and functionality of ionic liquid mixtures for diverse industrial processes, where the strength and nature of hydrogen bonds play a vital role.

3.1.5. Extraction of 1,3-PDO from aqueous phase to IL phase:

MD simulation was carried out to study the extraction of 1,3-PDO from the aqueous phase (raffinate phase) to IL phase (extract phase). Table S12 shows the distribution of molecules

between the extract and raffinate phases. Table 5 shows the mole fraction of components in the extract and raffinate phases. The extraction capability of a solvent are generally expressed in terms of distribution co-efficient (β) and selectivity (S) which are defined by the following expressions:

$$\boldsymbol{\beta = \frac{x^{E}_{PDO}}{x^{R}_{PDO}}} \tag{8}$$

$$\boldsymbol{S = \frac{x^{E}_{PDO}/x^{R}_{PDO}}{x^{E}_{Water}/x^{R}_{Water}}} \tag{9}$$

where x^{E}_{PDO} is the mole fraction of 1,3-PDO in extract phase and x^{R}_{PDO} is the mole fraction of 1,3-PDO in raffinate aqueous phase. x^{E}_{water} and x^{E}_{water} are the mole fraction of water in extract and raffinate respectively.

The distribution coefficient provides a quantification of the solutes' preference for each phase involved in the separation. It is desirable for the distribution coefficient of a solute to be sufficiently high, reducing the need for a higher solvent to feed ratio. The distribution coefficient of 1,3-PDO were in the range of 1-2 for [Bmim][NPF2] and [Bmim][NTF2] while for [Bmim][SCN] and [Bmim][TFO] were in the range of 12-15. It suggests 1,3-PDO can be extracted efficiently from the aqueous phase using [Bmim][SCN] and [Bmim][TFO]. The selectivity must be greater than unity for a useful extraction of solute using a solvent. The selectivity was in the range of 1.15 – 2.29 with [Bmim][NPF2] and [Bmim][NTF2] while it approximately 29 with [Bmim][SCN] and [Bmim][TFO]. The higher selectivity suggest that lesser stages are required to achieve the desired separation of the 1,3-PDO from the aqueous solution. Therefore, [Bmim][SCN] demonstrates the highest extraction efficiency in terms of distribution coefficient and selectivity, closely followed by [Bmim][TFO]. However, [Bmim][NPF2] and [Bmim][NTF2] exhibit limited suitability for the extraction of 1,3-PDO. Figure 8a-d depicts the snapshot of 1,3-PDO transfer from the raffinate phase to the extract phase. These results are in line with the observations obtained by the RDF and CDF studies based on the binary mixture of ILs and 1,3-PDO.

3.2 COSMO-SAC prediction:

The sigma profiles of the components involved in this study were calculated to understand the possible interactions between 1,3-PDO and ILs (Figure 9). The sigma profiles are divided into three regions: H-bond donor ($\sigma < -0.01$ e/Å^2), non-polar region (-0.01 e/Å$^2 < \sigma < +0.01$ e/Å^2) and H-bond acceptor ($\sigma > +0.01$ e/Å^2) regions. The sigma profile of 1,3-PDO is relatively symmetrical and wide which shows its ability to function both as a H-bond donor and H-bond acceptor. The sigma profiles of all the ILs are also distributed in all the three different regions. In H-bond donor region, all the ILs display identical σ-profile with less spread. However, [Bmim][SCN] has more spread in the H-bond acceptor region followed by [Bmim][TFO]. This shows the ability of these ILs to function as superior H-bond acceptors in comparison to [Bmim][NPF2] and [Bmim][NTF2]. Analyzing the σ-profile, it can be inferred that the interaction between 1,3-PDO and [Bmim][SCN] as well as between 1,3-PDO and [Bmim][TFO] is more favourable when compared to [Bmim][NPF2] and [Bmim][NTF2].

The COSMO-SAC model can also predict the infinite dilution activity coefficient, a crucial thermodynamic property. A lower value of this coefficient indicates stronger interactions between the components. The logarithmic infinite dilution activity coefficient (ln-gamma) values for 1,3-PDO in ILs is shown in Figure 10. Based on these it can be inferred that 1,3-PDO has strongest interaction with [Bmim][SCN] followed by [Bmim][TFO], [Bmim][NTF2] and [Bmim][NPF2] successively.

4. Conclusion:

The Molecular Dynamics simulations in this study provided valuable insights into the interactions and performance of four distinct ionic liquids ([Bmim][NTF2], [Bmim][NPF2], [Bmim][SCN], and [Bmim][TFO]) as potential extraction agents for 1,3-PDO. The deviation between simulated and experimental data, within a ±0.8 charge scaling range, yielded a favorable agreement with an ARD of 0.51%, indicating a small average percentage difference. The RDF analysis indicates an increased coordination number of 1,3-PDO around both the $[SCN]^-$ and the $[Bmim]^+$. This suggests a stronger interaction and a greater presence of 1,3-PDO molecules in the vicinity of [Bmim][SCN]. The SDF results indicate a high-density distribution of 1,3-PDO around [Bmim][SCN] and [Bmim][TFO], demonstrating a denser concentration compared to [Bmim][NPF2] and [Bmim][NTF2]. The comparative analysis of RDF and SDF data reveals intricate interactions, particularly evident as [Bmim][TFO] and [Bmim][SCN] display more

pronounced RDF anion peaks compared to [Bmim][NPF2] and [Bmim][NTF2]. This underscores the influential role of their respective anions ($[TFO]^-$ and $[SCN]^-$) in shaping interactions with 1,3-PDO. The increased RDF anion peaks imply more significant hydrogen bonding interactions with 1,3-PDO. This is further validated by quantifying the number of hydrogen bonds between ionic liquids (ILs) and 1,3-propanediol (1,3-PDO). Both [Bmim][NPF2] and [Bmim][NTF2], featuring non-coordinating anions ([NPF2]- and [NTF2]-), form an average of 0.654 and 0.952 hydrogen bonds with 1,3-propanediol. In contrast, [Bmim][SCN] exhibits the highest total number of hydrogen bonds (1.639) with 1,3-propanediol. This is attributed to [Bmim][SCN] containing the coordinating anion [SCN]-, which possesses a sulfur atom capable of forming hydrogen bonds with the [OH]- groups of 1,3-propanediol. The results from the ternary system indicate that [Bmim][SCN] and [Bmim][TFO] are highly efficient for the extraction of 1,3-PDO. Their performance surpasses that of [Bmim][NPF2] and [Bmim][NTF2], with distribution coefficients that are 10 to 20 times superior. Additionally, the selectivity for [Bmim][SCN] is 29, and for [Bmim][TFO] is 28.59, further highlighting their effectiveness.

COSMO-SAC has validated the results of the MD simulation. Infinite dilution activity coefficient values demonstrate that 1,3-PDO exhibits the strongest interaction with [Bmim][SCN] < [Bmim][TFO] << [Bmim][NTF2] < [Bmim][NPF2], further emphasizing the model's accuracy in characterizing the interaction strengths.

In conclusion, this study significantly advances our understanding of the complex interactions within IL-1,3-PDO systems and highlights the potential applications of these ionic liquids in extraction processes. The consistent trend observed across all analysis positions [Bmim][SCN] as the most promising ionic liquid for the extraction of 1,3-propanediol, followed by [Bmim][TFO], [Bmim][NTF2], and [Bmim][NPF2]. By systematically varying the anions while maintaining the $[Bmim]^+$ cation, the research offers valuable insights into how the choice of anions shapes the properties of ionic liquids in specific interactions, such as the extraction of 1,3-PDO.

References:

1. Saxena RK, Anand P, Saran S, Isar J. Microbial production of 1,3-propanediol: Recent developments and emerging opportunities. Biotechnol Adv. 2009 Aug;27(6):895–913.
2. da Silva Ruy AD, de Brito Alves RM, Reis Hewer TL, de Aguiar Pontes D, Gomes Teixeira LS, Magalhães Pontes LA. Catalysts for glycerol hydrogenolysis to 1,3-propanediol: A review of chemical routes and market. Catal Today. 2021 Dec 1;381:243–53.
3. Kurian J V. A new polymer platform for the future - Sorona® from corn derived 1,3-propanediol. J Polym Environ. 2005 Apr;13(2):159–67.
4. Xiu ZL, Zeng AP. Present state and perspective of downstream processing of biologically produced 1,3-propanediol and 2,3-butanediol. Vol. 78, Applied Microbiology and Biotechnology. 2008. p. 917–26.
5. Boonsongsawat T, Shotipruk A, Tantayakom V, Prasitchoke P, Chandavasu C, Boonnoun P, et al. Solvent extraction of biologically derived 1,3-propanediol with ethyl acetate and ethanol cosolvent. Sep Sci Technol. 2010 Jan;45(4):541–7.
6. Hao J, Sun Y, Wang Q, Tong X, Zhang H, Zhang Q. Effect and mechanism of penetration enhancement of organic base and alcohol on Glycyrrhetinic acid in vitro. Int J Pharm. 2010 Oct;399(1–2):102–8.
7. Boonoun P, Laosiripojana N, Muangnapoh C, Jongsomjit B, Panpranot J, Mekasuwandumrong O, et al. Application of sulfonated carbon-based catalyst for reactive extraction of 1,3-propanediol from model fermentation mixture. Ind Eng Chem Res. 2010 Dec 15;49(24):12352–7.
8. Hao J, Liu H, Liu D. Novel route of reactive extraction to recover 1,3-propanediol from a dilute aqueous solution. Ind Eng Chem Res. 2005 Jun 8;44(12):4380–5.
9. Gao S, Zhang D, Sun Y, Xiu Z. Separation of 1,3-propanediol from glycerol-based fermentations of Klebsiella pneumoniae by alcohol precipitation and dilution crystallization. Frontiers of Chemical Engineering in China. 2007 May;1(2):202–7.
10. US6479716.
11. Gong Y, Tang Y, Wang XL, Yu LX, Liu DH. The possibility of the desalination of actual 1,3-propanediol fermentation broth by electrodialysis. Vol. 16, Desalination. 2004.
12. Song Z, Sun Y, Wei B, Xiu Z. Two-step salting-out extraction of 1,3-propanediol and lactic acid from the fermentation broth of Klebsiella pneumoniae on biodiesel-derived crude glycerol. Eng Life Sci. 2013 Sep;13(5):487–95.
13. cui C, Zhang Z, Chen B. Environmentally-friendly strategy for separation of 1,3-propanediol using biocatalytic conversion. Bioresour Technol. 2017;245:477–82.
14. Barski P, Kowalczyk J, Lindstaedt A, Puzewicz-Barska J, Witt D. Evaluation of solid phase extraction for downstream separation of propane-1,3-diol and butan-1-ol from fermentation broth. Process Biochemistry. 2012 Jun;47(6):1005–10.
15. Li Z, Yan L, Zhou J, Wang X, Sun Y, Xiu ZL. Two-step salting-out extraction of 1,3-propanediol, butyric acid and acetic acid from fermentation broths. Sep Purif Technol. 2019 Jan 31;209:246–53.
16. cui C, Zhang Z, Chen B. Environmentally-friendly strategy for separation of 1,3-propanediol using biocatalytic conversion. Bioresour Technol. 2017;245:477–82.
17. Gao S, Zhang D, Sun Y, Xiu Z. Separation of 1,3-propanediol from glycerol-based fermentations of Klebsiella pneumoniae by alcohol precipitation and dilution crystallization. Frontiers of Chemical Engineering in China. 2007 May;1(2):202–7.

18. Anand P, Saxena RK, Marwah RG. A novel downstream process for 1,3-propanediol from glycerol-based fermentation. Appl Microbiol Biotechnol. 2011 May;90(4):1267–76.
19. Barski P, Kowalczyk J, Lindstaedt A, Puzewicz-Barska J, Witt D. Evaluation of solid phase extraction for downstream separation of propane-1,3-diol and butan-1-ol from fermentation broth. Process Biochemistry. 2012 Jun;47(6):1005–10.
20. Sui WB, Sun YQ, Wang XL, Xiu ZL. Synergistic Extraction of 1,3-Propanediol from Fermentation Broths Using Multialcohol Extractants. ACS Sustain Chem Eng. 2022 Sep 12;10(36):11891–901.
21. Wasserscheid P, Welton T. Ionic Liquids in Synthesis: Second Edition. Ionic Liquids in Synthesis: Second Edition . 2008 Aug;1:1–721. Available from: https://onlinelibrary.wiley.com/doi/book/10.1002/9783527621194
22. Zhu Z, Ri Y, Li M, Jia H, Wang Y, Wang Y. Extractive distillation for ethanol dehydration using imidazolium-based ionic liquids as solvents. Chemical Engineering and Processing - Process Intensification. 2016 Aug;109:190–8.
23. Zante G, Masmoudi A, Barillon R, Trébouet D, Boltoeva M. Separation of lithium, cobalt and nickel from spent lithium-ion batteries using TBP and imidazolium-based ionic liquids. Journal of Industrial and Engineering Chemistry. 2020 Aug;82:269–77.
24. Wan T, Zhou L, Gong K, Zhang K, Zhang J, Wang X, et al. Molecular insights into the separation mechanism of imidazole-based ionic liquid supported membranes. J Mol Liq. 2021 Aug;340:117173.
25. Xu D, He S, Yuan C, Peng L, Fan W, Huang H, et al. Liquid-liquid equilibrium and insights of intermolecular interactions for separation of isopropyl acetate + isopropanol by imidazolium-based ionic liquids. J Taiwan Inst Chem Eng. 2022 Aug;140:104571.
26. Zhao D, Xiong Y, Wang Y, Lu B, Zhang H. Separation of anthracene and carbazole from crude anthracene via imidazolium-based ionic liquids. Fuel. 2023 Aug;331:125704.
27. Zhang X, Wang Z, Wang K, Reyes-Labarta JA, Gao J, Xu D, et al. Liquid-liquid phase equilibrium and interaction exploration for separation of azeotrope (2,2,3,3-tetrafluoro-1-propanol + water) with two imidazolium-based ionic liquids. J Mol Liq. 2020 Aug;300:112266.
28. Zhu Z, Bai W, Xu Y, Gong H, Wang Y, Xu D, et al. Liquid-liquid extraction of methanol from its mixtures with hexane using three imidazolium-based ionic liquids. J Chem Thermodyn. 2019 Aug;138:189–95.
29. Wang P, Yan P, Reyes-Labarta JA, Gao J, Xu D, Zhang L, et al. Liquid-liquid measurement and correlation for separation of azeotrope (dimethyl carbonate and ethanol) with different imidazolium-based ionic liquids. Fluid Phase Equilib. 2019 Aug;485:183–9.
30. Li A, Xu X, Zhang L, Gao J, Xu D, Wang Y. Separation of cresol from coal tar by imidazolium-based ionic liquid [Emim][SCN]: Interaction exploration and extraction experiment. Fuel. 2020 Aug;264:116908.
31. Wang P, Xu D, Yan P, Gao J, Zhang L, Wang Y. Separation of azeotrope (ethanol and ethyl methyl carbonate) by different imidazolium-based ionic liquids: Ionic liquids interaction analysis and phase equilibrium measurements. J Mol Liq. 2018 Aug;261:89–95.
32. Corderí S, González EJ, Calvar N, Domínguez Á. Application of [HMim][NTf2], [HMim][TfO] and [BMim][TfO] ionic liquids on the extraction of toluene from alkanes: Effect of the

anion and the alkyl chain length of the cation on the LLE. J Chem Thermodyn. 2012 Aug;53:60–6.
33. Chapeaux A, Simoni LD, Ronan TS, Stadtherr MA, Brennecke JF. Extraction of alcohols from water with 1-hexyl-3-methylimidazolium bis(trifluoromethylsulfonyl)imide. Green Chemistry . 2008 Aug;10(12):1301–6. Available from: https://pubs.rsc.org/en/content/articlehtml/2008/gc/b807675h
34. Ha SH, Mai NL, Koo YM. Butanol recovery from aqueous solution into ionic liquids by liquid-liquid extraction. Process Biochemistry. 2010 Dec;45(12):1899–903.
35. Nann A, Held C, Sadowski G. Liquid-liquid equilibria of 1-butanol/water/IL systems. Ind Eng Chem Res. 2013 Dec 26;52(51):18472–81.
36. Müller A, Górak A. Extraction of 1,3-propanediol from aqueous solutions using different ionic liquid-based aqueous two-phase systems. In: Separation and Purification Technology. 2012. p. 130–6.
37. Zhu Z, Xu Y, Li H, Shen Y, Meng D, Cui P, et al. Separation of isopropyl alcohol and isopropyl ether with ionic liquids as extractant based on quantum chemical calculation and liquid-liquid equilibrium experiment. 2020; Available from: https://doi.org/10.1016/j.seppur.2020.116937
38. Mosallanejad MR, Khosravi-Nikou MR, Shariati A. Separation of ethanol from n-decane-ethanol mixtures using imidazolium based ionic liquids. 2018; Available from: https://doi.org/10.1016/j.jct.2018.11.027
39. Cumplido P, Cháfer A, Torre JD La, Poy H. Separation of the azeotropic mixture 2-propanol + water employing different imidazolium ionic liquids as solvents. 2019; Available from: https://doi.org/10.1016/j.jct.2019.105889
40. Monjur MS, Iftakher A, Hasan MMF. Separation Process Synthesis for High-GWP Refrigerant Mixtures: Extractive Distillation using Ionic Liquids. Ind Eng Chem Res . 2022 Aug;61(12):4390–406. Available from: https://pubs.acs.org/doi/abs/10.1021/acs.iecr.2c00136
41. Makowska A, Dyoniziak E, Siporska A, Szydłowski J. Miscibility of ionic liquids with polyhydric alcohols. Journal of Physical Chemistry B . 2010 Sep;114(7):2504–8. Available from: https://pubs.acs.org/doi/full/10.1021/jp911660a
42. Nian B, Cao C, Liu Y. Lipase and Metal Chloride Hydrate-Natural Deep Eutectic Solvents Synergistically Catalyze Amidation Reaction via Multiple Noncovalent Bond Interactions. ACS Sustain Chem Eng . 2019 Aug;7(21):18174–84. Available from: https://pubs.acs.org/doi/full/10.1021/acssuschemeng.9b05691
43. Zhu Z, Bai W, Xu Y, Gong H, Wang Y, Xu D, et al. Liquid-liquid extraction of methanol from its mixtures with hexane using three imidazolium-based ionic liquids. J Chem Thermodyn. 2019 Nov 1;138:189–95.
44. Banerjee T, Paul N, Naik PK, Ribeiro BD, Pattader PSG, Marrucho IM. Molecular dynamics insights and water stability of hydrophobic deep eutectic solvents aided extraction of nitenpyram from an aqueous environment. Journal of Physical Chemistry B . 2020;124(34):7405–20. Available from: https://pubs.acs.org/doi/full/10.1021/acs.jpcb.0c03647

45. Naik PK, Mohan M, Banerjee T, Paul S, Goud V V. Molecular Dynamic Simulations for the Extraction of Quinoline from Heptane in the Presence of a Low-Cost Phosphonium-Based Deep Eutectic Solvent. Journal of Physical Chemistry B. 2018 Apr 12;122(14):4006–15.
46. Zhu Z, Li H, Xu Y, Zhang W, Shen Y, Gao J, et al. Quantum chemical calculation, molecular dynamics simulation and process design for separation of heptane - butanol using ionic liquids extraction. J Mol Liq. 2020 Oct 10;316:113851.
47. Wang X, Gu X, Murad S. Molecular dynamics simulations of liquid-liquid phase equilibrium of ternary methanol/water/hydrocarbon mixtures. Fluid Phase Equilib. 2018 Aug 25;470:109–19.
48. Li J, Wang J, Wu M, Cheng H, Chen L, Qi Z. Deep Deterpenation of Citrus Essential Oils Intensified by In Situ Formation of a Deep Eutectic Solvent in Associative Extraction. 2020 May 13; Available from: /articles/journal_contribution/Deep_Deterpenation_of_Citrus_Essential_Oils_Intensified_by_In_Situ_Formation_of_a_Deep_Eutectic_Solvent_in_Associative_Extraction/12231125/1
49. Lin ST, Sandler SI. A Priori Phase Equilibrium Prediction from a Segment Contribution Solvation Model. Ind Eng Chem Res . 2001 Mar 6;41(5):899–913. Available from: https://pubs.acs.org/doi/abs/10.1021/ie001047w
50. Xiong R, Sandler SI, Burnett RI. An Improvement to COSMO-SAC for Predicting Thermodynamic Properties. Ind Eng Chem Res. 2014 May 14;53(19):8265–78.
51. Chen WL, Hsieh CM, Yang L, Hsu CC, Lin ST. A Critical Evaluation on the Performance of COSMO-SAC Models for Vapor-Liquid and Liquid-Liquid Equilibrium Predictions Based on Different Quantum Chemical Calculations. Ind Eng Chem Res . 2016 Aug 31 ;55(34):9312–22. Available from: https://pubs.acs.org/doi/full/10.1021/acs.iecr.6b02345
52. Mullins E, Oldland R, Liu YA, Wang S, Sandler SI, Chen CC, et al. Sigma-Profile Database for Using COSMO-Based Thermodynamic Methods. Ind Eng Chem Res. 2006 Jun 7;45(12):4389–415.
53. Meng X, Li R, Bing X, Gao J, Xu D, Zhang L, et al. Liquid-liquid equilibrium measurements and interaction exploration for separation of isobutyl alcohol + isobutyl acetate by imidazolium-based ionic liquids with different anions. J Chem Thermodyn. 2020 Feb 1;141:105932.
54. Shah MR, Yadav GD. Prediction of liquid-liquid equilibria for biofuel applications by quantum chemical calculations using the Cosmo-SAC method. Ind Eng Chem Res . 2011 Dec 7;50(23):13066–75. Available from: https://pubs.acs.org/doi/abs/10.1021/ie201454m
55. Zhang L, Zhang M, Gao J, Xu D, Zhou S, Wang Y. Efficient Extraction of Neutral Heterocyclic Nitrogen Compounds from Coal Tar via Ionic Liquids and Its Mechanism Analysis. Energy and Fuels . 2018 Sep 20; 32(9):9358–70. Available from: https://pubs.acs.org/doi/abs/10.1021/acs.energyfuels.8b02297
56. Bharti A, Verma R, Prerna, Sarvesh Namdeo, Malviya A, Banerjee T, et al. Liquid-liquid equilibria and COSMO-SAC modeling of organic solvent/ionic liquid - hydroxyacetone - water mixtures. Fluid Phase Equilib. 2018 Apr 25;462:73–84.

57. Jorgensen WL, Maxwell DS, Tirado-Rives J. Development and Testing of the OPLS All-Atom Force Field on Conformational Energetics and Properties of Organic Liquids . 1996. Available from: https://pubs.acs.org/sharingguidelines
58. Doherty B, Zhong X, Gathiaka S, Li B, Acevedo O. Revisiting OPLS Force Field Parameters for Ionic Liquid Simulations. J Chem Theory Comput. 2017 Dec 12;13(12):6131–5.
59. Udier-Blagović M, Morales De Tirado P, Pearlman SA, Jorgensen WL. Accuracy of free energies of hydration using CM1 and CM3 atomic charges. J Comput Chem . 2004 Aug 1; 25(11):1322–32. Available from: https://onlinelibrary.wiley.com/doi/full/10.1002/jcc.20059
60. Dodda LS, Cabeza De Vaca I, Tirado-Rives J, Jorgensen WL. LigParGen web server: an automatic OPLS-AA parameter generator for organic ligands. Nucleic Acids Res . 2017; 45:331–6. Available from: https://academic.oup.com/nar/article/45/W1/W331/3747780
61. Dodda LS, Vilseck JZ, Tirado-Rives J, Jorgensen WL. 1.14∗CM1A-LBCC: Localized Bond-Charge Corrected CM1A Charges for Condensed-Phase Simulations. Journal of Physical Chemistry B . 2017 Apr 2; 121(15):3864–70. Available from: https://pubs.acs.org/doi/pdf/10.1021/acs.jpcb.7b00272
62. Vassetti D, Pagliai M, Procacci P. Assessment of GAFF2 and OPLS-AA General Force Fields in Combination with the Water Models TIP3P, SPCE, and OPC3 for the Solvation Free Energy of Druglike Organic Molecules. J Chem Theory Comput . 2019 Mar 12; 15(3):1983–95. Available from: https://pubs.acs.org/doi/abs/10.1021/acs.jctc.8b01039
63. Martinez L, Andrade R, Birgin EG, Martínez JM. PACKMOL: A package for building initial configurations for molecular dynamics simulations. J Comput Chem. 2009;30(13):2157–64.
64. Li K, Lin X, Greenberg J. Software citation, reuse and metadata considerations: An exploratory study examining LAMMPS. Proceedings of the Association for Information Science and Technology. 2016;53(1):1–10.
65. Yue K, Doherty B, Acevedo O. Comparison between Ab Initio Molecular Dynamics and OPLS-Based Force Fields for Ionic Liquid Solvent Organization. Journal of Physical Chemistry B. 2022 Jun 2;126(21):3908–19.
66. Luty BA, Davis ME, Tironi IG, Van Gunsteren WF. A Comparison of Particle-Particle, Particle-Mesh and Ewald Methods for Calculating Electrostatic Interactions in Periodic Molecular Systems. http://dx.doi.org/101080/08927029408022004 . 2006; 14(1):11–20. Available from: https://www.tandfonline.com/doi/abs/10.1080/08927029408022004
67. Nosé S, Klein ML. A study of solid and liquid carbon tetrafluoride using the constant pressure molecular dynamics technique. J Chem Phys . 1983 Jun 1; 78(11):6928–39. Available from: /aip/jcp/article/78/11/6928/439000/A-study-of-solid-and-liquid-carbon-tetrafluoride
68. Hoover WG. Canonical dynamics: Equilibrium phase-space distributions. Phys Rev A (Coll Park) . 1985 Mar 1; 31(3):1695. Available from: https://journals.aps.org/pra/abstract/10.1103/PhysRevA.31.1695
69. Parrinello M, Rahman A. Polymorphic transitions in single crystals: A new molecular dynamics method. J Appl Phys . 1981 Dec 1; 52(12):7182–90. Available from: /aip/jap/article/52/12/7182/9558/Polymorphic-transitions-in-single-crystals-A-new

70. Brehm M, Thomas M, Gehrke S, Kirchner B. TRAVIS—A free analyzer for trajectories from molecular simulation. Journal of Chemical Physics . 2020 Sep;152(16):164105. Available from: /aip/jcp/article/152/16/164105/198859/TRAVIS-A-free-analyzer-for-trajectories-from
71. Humphrey W, Dalke A, Schulten K. VMD – Visual Molecular Dynamics. J Mol Graph. 1996;14:33–8.
72. Mark P, Nilsson L. Structure and dynamics of the TIP3P, SPC, and SPC/E water models at 298 K. Journal of Physical Chemistry A . 2001 Nov 1; 105(43):9954–60. Available from: https://pubs.acs.org/doi/full/10.1021/jp003020w
73. Working with water in LAMMPS - Christopher O'Brien, Ph.D. Available from: https://sites.google.com/a/ncsu.edu/cjobrien/tutorials-and-guides/working-with-water-in-lammps
74. Klamt A. Conductor-like screening model for real solvents: A new approach to the quantitative calculation of solvation phenomena. Journal of Physical Chemistry . 1995; 99(7):2224–35. Available from: https://pubs.acs.org/doi/abs/10.1021/j100007a062
75. Klamt A, Jonas V, Bürger T, Lohrenz JCW. Refinement and parametrization of COSMO-RS. Journal of Physical Chemistry A . 1998 Jun 25; 102(26):5074–85. Available from: https://pubs.acs.org/doi/full/10.1021/jp980017s
76. Klamt A, Eckert F. COSMO-RS: a novel and efficient method for the a priori prediction of thermophysical data of liquids. Fluid Phase Equilib. 2000 Jul 28;172(1):43–72.
77. Klamt A, Lin ST, Sandler SI. Comments on 'A priori phase equilibrium prediction from a segment contribution solvation model' (Multiple letters). Ind Eng Chem Res . 2002 May 1; 41(9):2330–4. Available from: https://pubs.acs.org/doi/full/10.1021/ie011031l
78. Hanwell MD, Curtis DE, Lonie DC, Vandermeerschd T, Zurek E, Hutchison GR. Avogadro: an advanced semantic chemical editor, visualization, and analysis platform. J Cheminform . 2012 Aug; 4(1). Available from: https://pubmed.ncbi.nlm.nih.gov/22889332/
79. Frisch MJ, Trucks GW, Schlegel HB, Scuseria GE, Robb MA, Cheeseman JR, et al. Gaussian˜16 Revision C.01. 2016.
80. Lee C, Yang W, Parr RG. Development of the Colle-Salvetti correlation-energy formula into a functional of the electron density. Phys Rev B . 1988 Jan 15; 37(2):785. Available from: https://journals.aps.org/prb/abstract/10.1103/PhysRevB.37.785
81. Becke AD. Density-functional thermochemistry. III. The role of exact exchange. Journal of Chemical Physics. 1993;98(7):5648–52.
82. Stephens PJ, Devlin FJ, Chabalowski CF, Frisch MJ. Ab Initio calculation of vibrational absorption and circular dichroism spectra using density functional force fields. Journal of Physical Chemistry® . 1994; 98(45):11623–7. Available from: https://pubs.acs.org/doi/abs/10.1021/j100096a001
83. Anantharaj R, Banerjee T. COSMO-RS-based screening of ionic liquids as green solvents in denitrification studies. Ind Eng Chem Res . 2010 Sep 15; 49(18):8705–25. Available from: https://pubs.acs.org/doi/full/10.1021/ie901341k
84. Bell IH, Mickoleit E, Hsieh CM, Lin ST, Vrabec J, Breitkopf C, et al. A Benchmark Open-Source Implementation of COSMO-SAC. J Chem Theory Comput . 2020 Apr 14; 16(4):2635–46. Available from: https://pubs.acs.org/doi/abs/10.1021/acs.jctc.9b01016

85. Doherty B, Zhong X, Gathiaka S, Li B, Acevedo O. Revisiting OPLS Force Field Parameters for Ionic Liquid Simulations. J Chem Theory Comput. 2017 Dec 12;13(12):6131–5.
86. Tokuda H, Ishii K, Susan MABH, Tsuzuki S, Hayamizu K, Watanabe M. Physicochemical properties and structures of room-temperature ionic liquids. 3. Variation of cationic structures. Journal of Physical Chemistry B. 2006 Feb 16;110(6):2833–9.
87. Yee P, Shah JK, Maginn EJ. State of hydrophobic and hydrophilic ionic liquids in aqueous solutions: Are the ions fully dissociated? Journal of Physical Chemistry B. 2013 Oct 17;117(41):12556–66.
88. Gonfa G, Bustam MA, Muhammad N, Khan AS. Evaluation of Thermophysical Properties of Functionalized Imidazolium Thiocyanate Based Ionic Liquids. Ind Eng Chem Res. 2015 Aug;54(49):12428–37.
89. Zhang R, Yue X, Li B, Yang J, Wu Z, Zhang J. Dynamic viscosity, density and surface tension of 1,3-propanediol (1) + 1,2-propanediamine (2) binary system at T = (293.15 to 318.15) K and atmosphere pressure. J Mol Liq. 2020 Feb 1;299.
90. Zhao Y, Gao S, Wang J, Tang J. Aggregation of ionic liquids [Cnmim]Br (n = 4, 6, 8, 10, 12) in D2O: A NMR study. Journal of Physical Chemistry B . 2008 Aug;112(7):2031–9. Available from: https://pubs.acs.org/doi/full/10.1021/jp076467e
91. Molecular Simulation/Radial Distribution Functions - Wikibooks, open books for an open world. Available from: https://en.wikibooks.org/wiki/Molecular_Simulation/Radial_Distribution_Functions
92. Paschek D, Golub B, Ludwig R. Hydrogen bonding in a mixture of protic ionic liquids: a molecular dynamics simulation study. Physical Chemistry Chemical Physics . 2015 Sep;17(13):8431–40. Available from: https://pubs.rsc.org/en/content/articlehtml/2015/cp/c4cp05432f
93. Zhu Z, Li H, Xu Y, Zhang W, Shen Y, Gao J, et al. Quantum chemical calculation, molecular dynamics simulation and process design for separation of heptane - butanol using ionic liquids extraction. J Mol Liq. 2020 Oct 10;316:113851.
94. Kumar N, Naik PK, Banerjee T. Molecular modeling insights in the extraction of benzene from hydrocarbon stream using deep eutectic solvent. J Mol Liq. 2020 Nov 1;317:113909.
95. Paul S, Paul S. The influence of trehalose on hydrophobic interactions of small nonpolar solute: A molecular dynamics simulation study. J Chem Phys . 2013 Jul 28; 139(4). Available from: https://pubmed.ncbi.nlm.nih.gov/23901994/
96. Pethes I, Bakó I, Pusztai L. Chloride ions as integral parts of hydrogen bonded networks in aqueous salt solutions: The appearance of solvent separated anion pairs. Physical Chemistry Chemical Physics. 2020 May 21;22(19):11038–44.
97. Domańska U, Królikowska M. Effect of temperature and composition on the surface tension and thermodynamic properties of binary mixtures of 1-butyl-3-methylimidazolium thiocyanate with alcohols. J Colloid Interface Sci. 2010 Aug 15;348(2):661–7.
98. Pereiro AB, Rodríguez A. Study on the phase behaviour and thermodynamic properties of ionic liquids containing imidazolium cation with ethanol at several temperatures. Journal of Chemical Thermodynamics. 2007 Jun;39(6):978–89.

Funding:

This study was conducted without the support of a dedicated grant from any funding agency, whether in the public, commercial, or not-for-profit sectors.

Figures

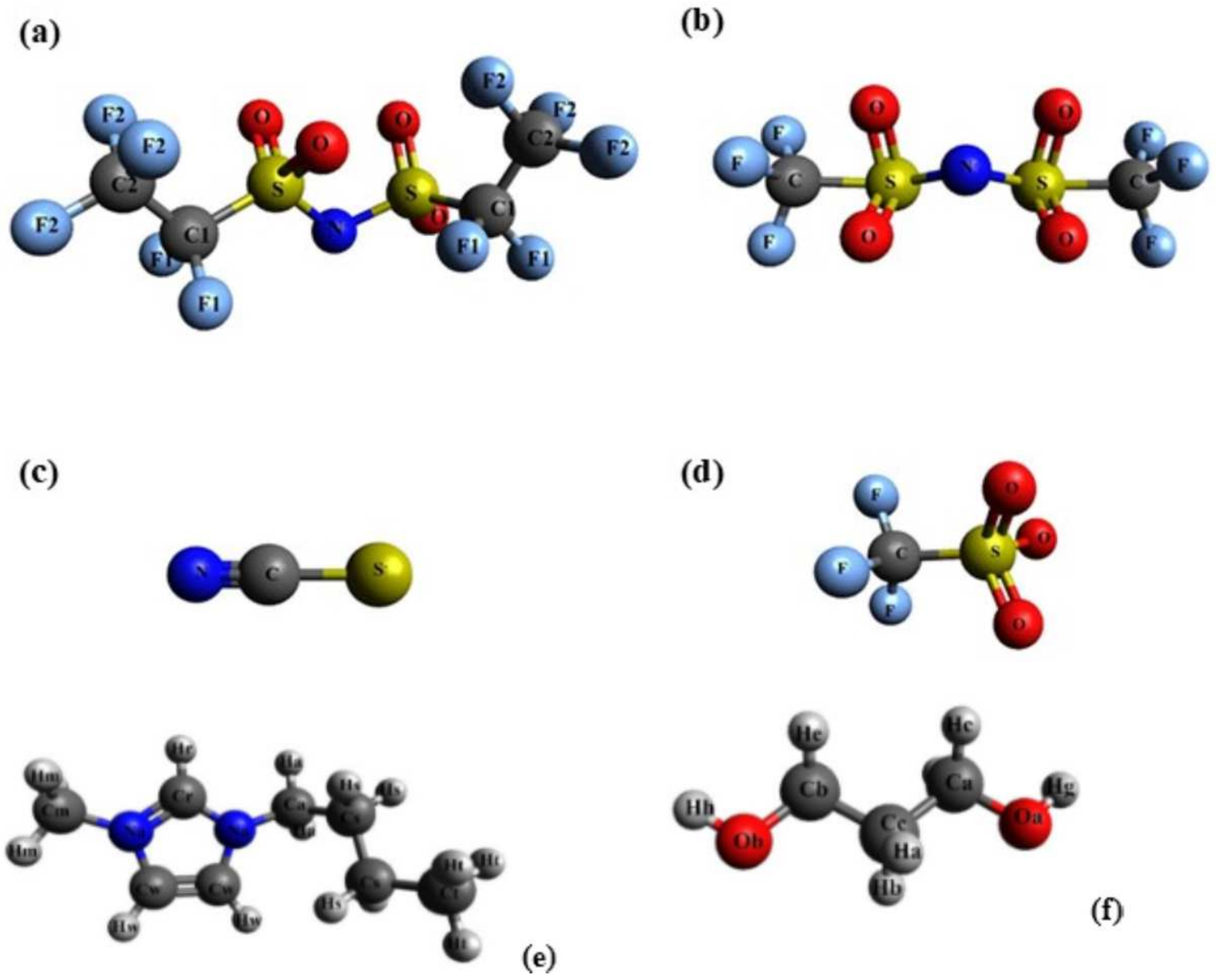

Figure 1

Chemical structures of the components, along with atom types used in this work. (a) Bis (pentafluoroethane sulfonyl)amide $[NPF2]^-$ (b) Bis[(trifluoromethyl)sulfonyl]imide $[NTF2]^-$ (c) Thiocyanate $[SCN]^-$ and (d) Trifluoromethanesulfonate $[TFO]^-$ (e) 1-butyl-3-methylimidazolium cation $[Bmim]^+$ (f) 1,3-Propanediol [1,3-PDO]

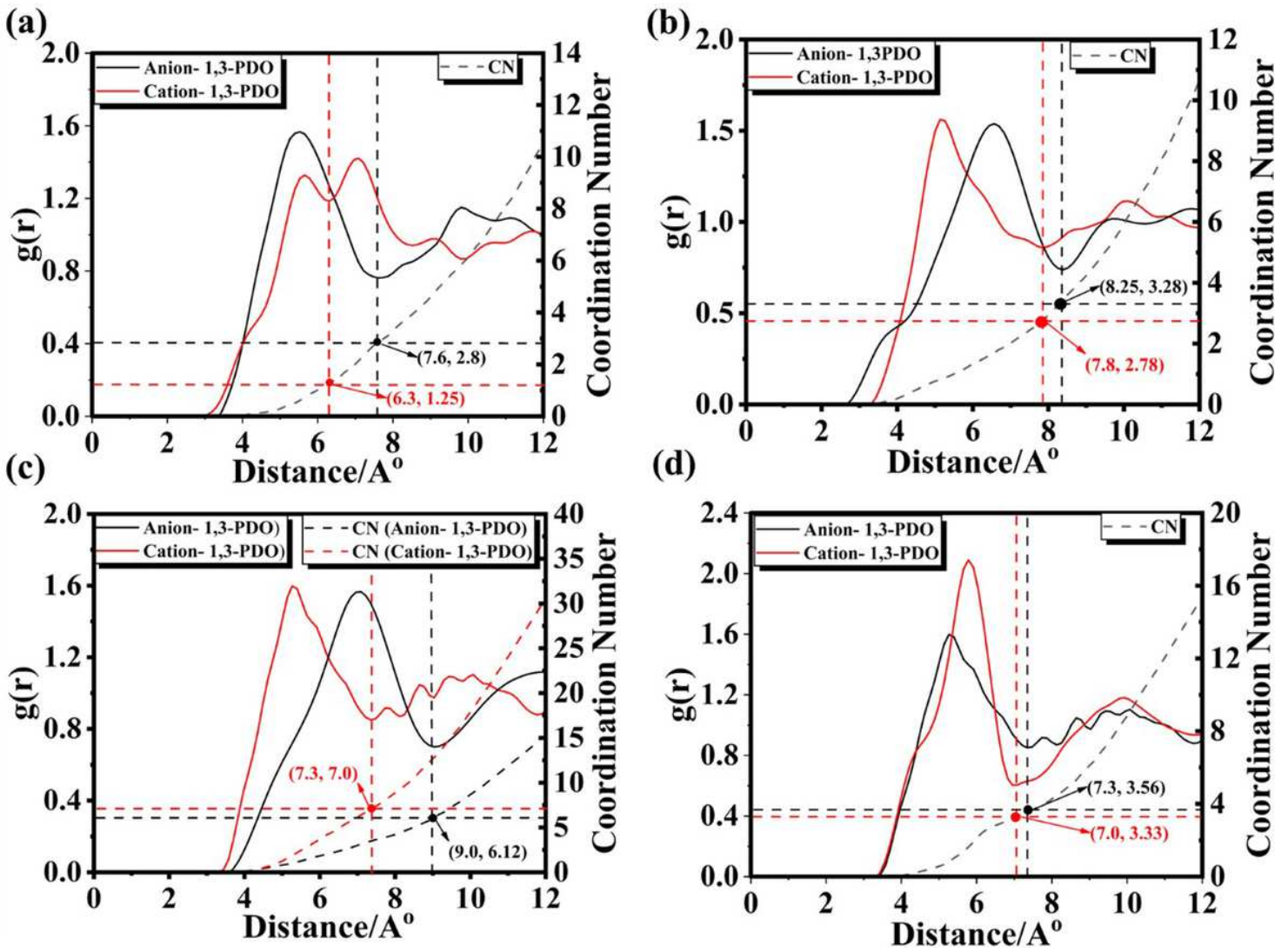

Figure 2

Radial distribution functions (RDFs) and coordination number (CN) between cation-1,3-PDO and anion-1,3-PDO. (a) [Bmim][NPF2]-1,3PDO, (b) [Bmim][NTF2]-1,3PDO, (c) [Bmim][SCN]-1,3PDO, and (d) [Bmim][TFO]-1,3PDO.

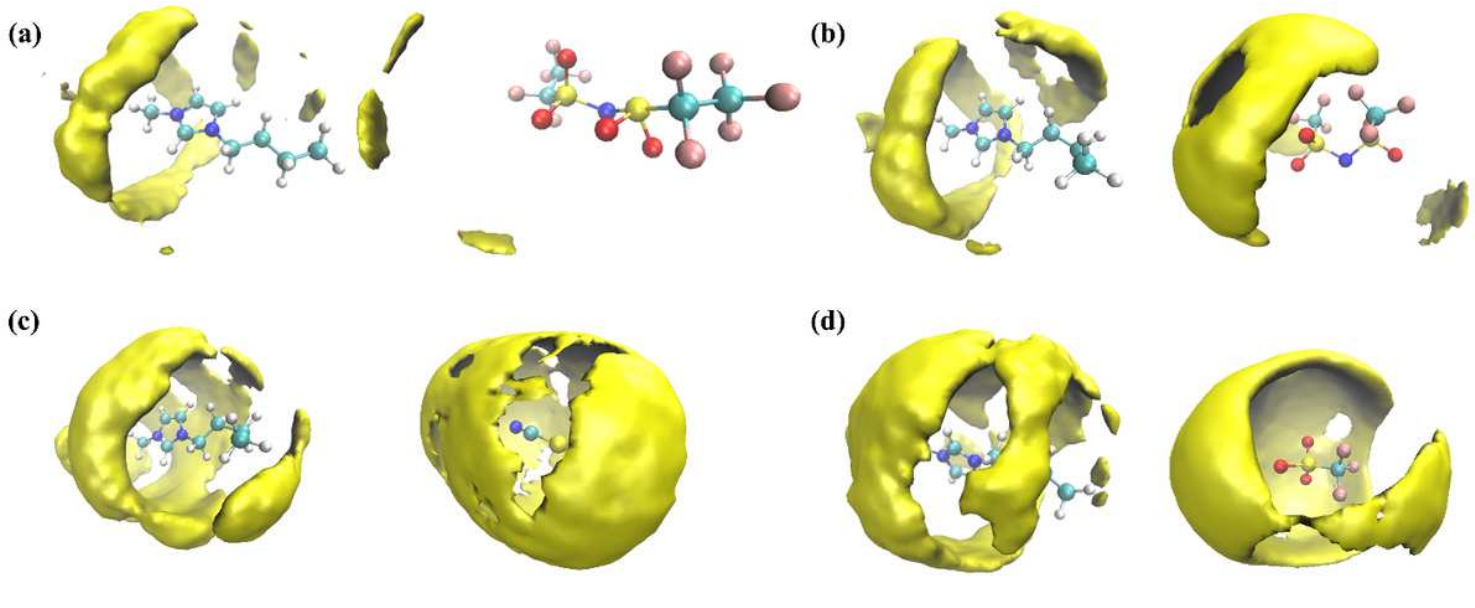

Figure 3

Spatial Distribution Function (SDF) visualizations of 1,3-PDO around different ILs. The yellow color indicates the presence of 1,3-PDO. (a) SDF of 1,3-PDO around [Bmim][NPF2], (b) SDF of 1,3-PDO around [Bmim][NTF2], (c) SDF of 1,3-PDO around [Bmim][SCN] and (d) SDF of 1,3-PDO around [Bmim][TFO].

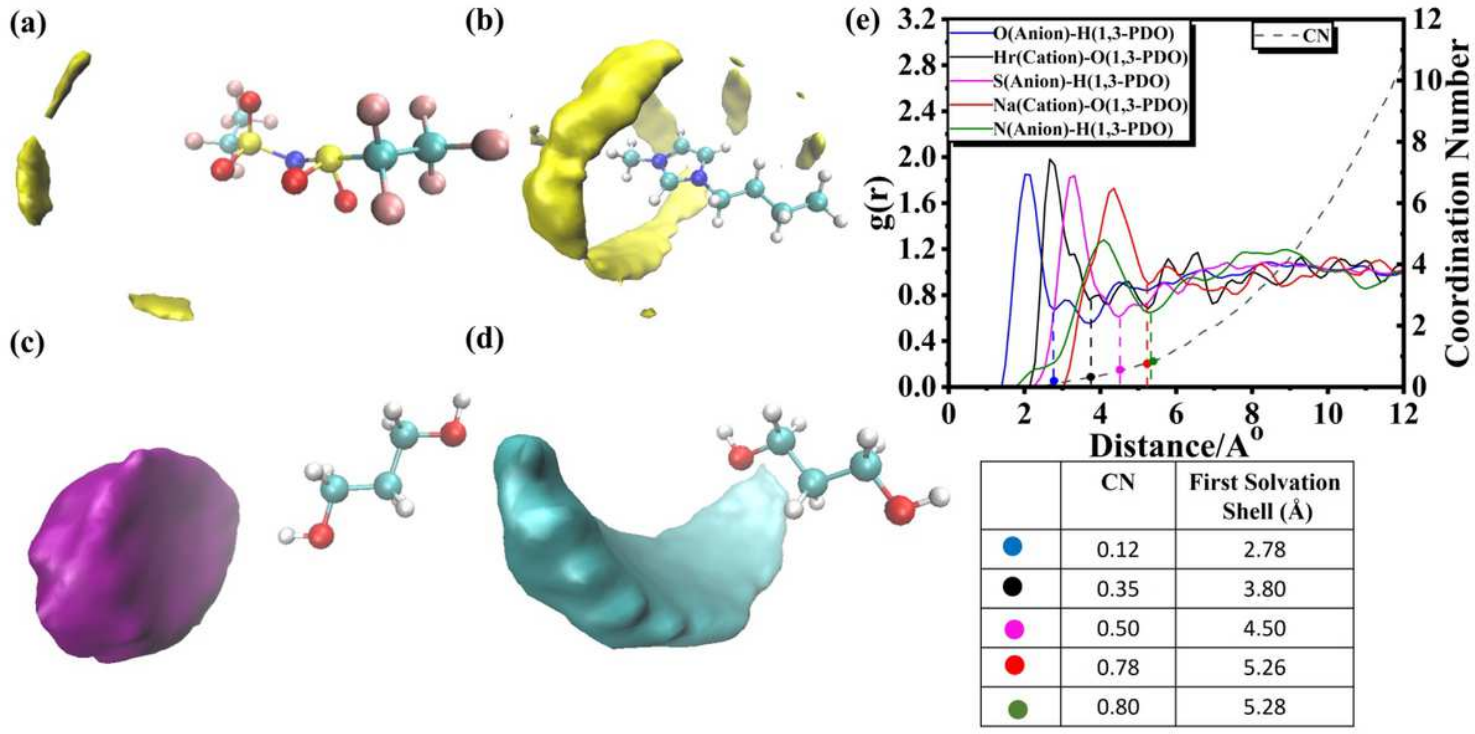

	CN	First Solvation Shell (Å)
●	0.12	2.78
●	0.35	3.80
●	0.50	4.50
●	0.78	5.26
●	0.80	5.28

Figure 4

Molecular Distribution Analysis and Interatomic RDF of [Bmim][NPF2] with 1,3-PDO. (a) SDF of 1,3-PDO around $[NPF2]^-$, (b) SDF of 1,3-PDO around $[Bmim]^+$, (c) SDF of $[NPF2]^-$ around 1,3-PDO, (d) SDF of

[Bmim]$^+$ around 1,3-PDO, and (e) Interatomic RDF Plot of ILs and 1,3-PDO at 298 K.

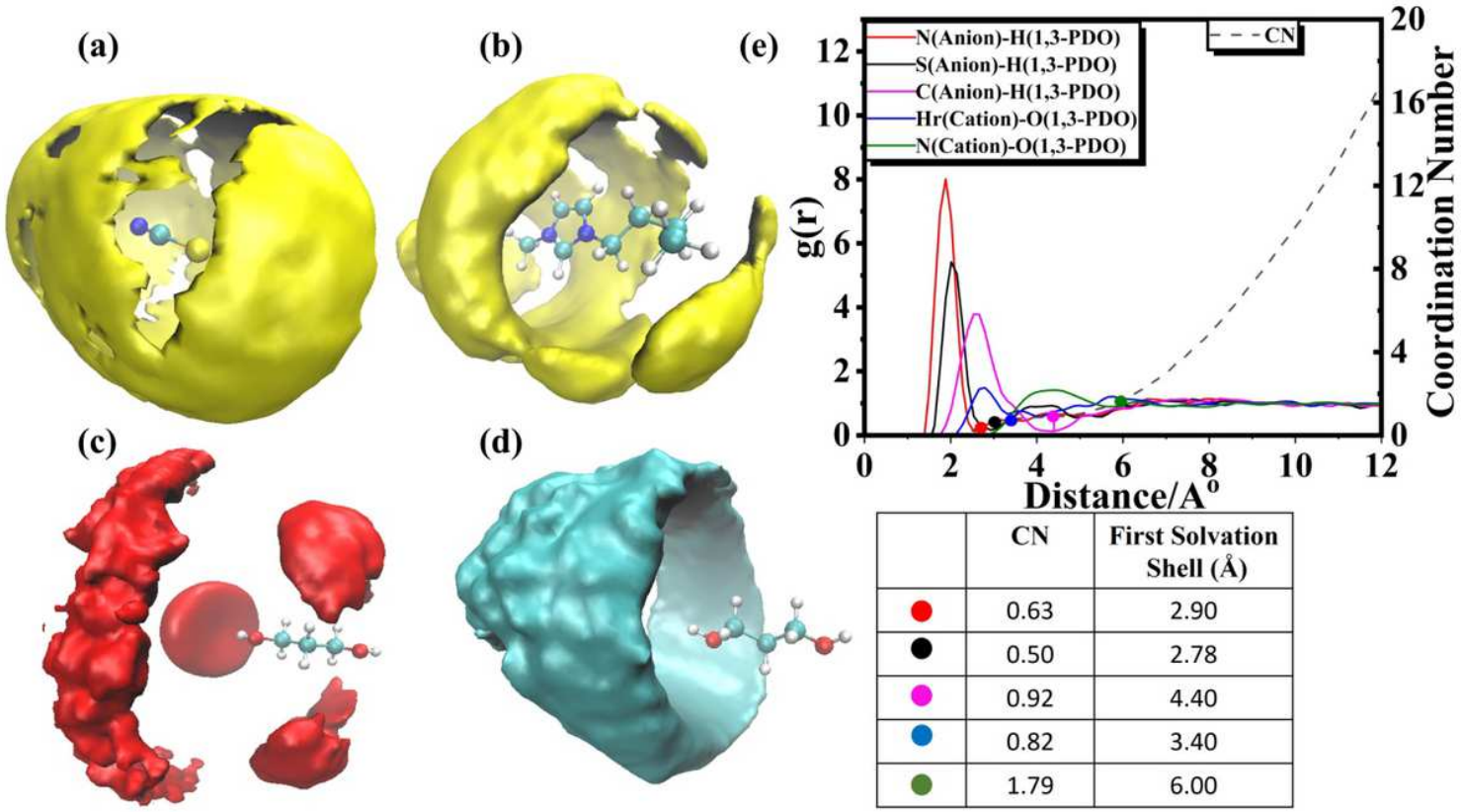

	CN	First Solvation Shell (Å)
●	0.63	2.90
●	0.50	2.78
●	0.92	4.40
●	0.82	3.40
●	1.79	6.00

Figure 5

Molecular Distribution Analysis and Interatomic RDF of [Bmim][SCN] with 1,3-PDO. (a) SDF of 1,3-PDO around [SCN]$^-$, (b) SDF of 1,3-PDO around [Bmim]$^+$, (c) SDF of [SCN]$^-$ around 1,3-PDO, (d) SDF of [Bmim]$^+$ around 1,3-PDO, and (e) Interatomic RDF Plot of ILs and 1,3-PDO at 298 K.

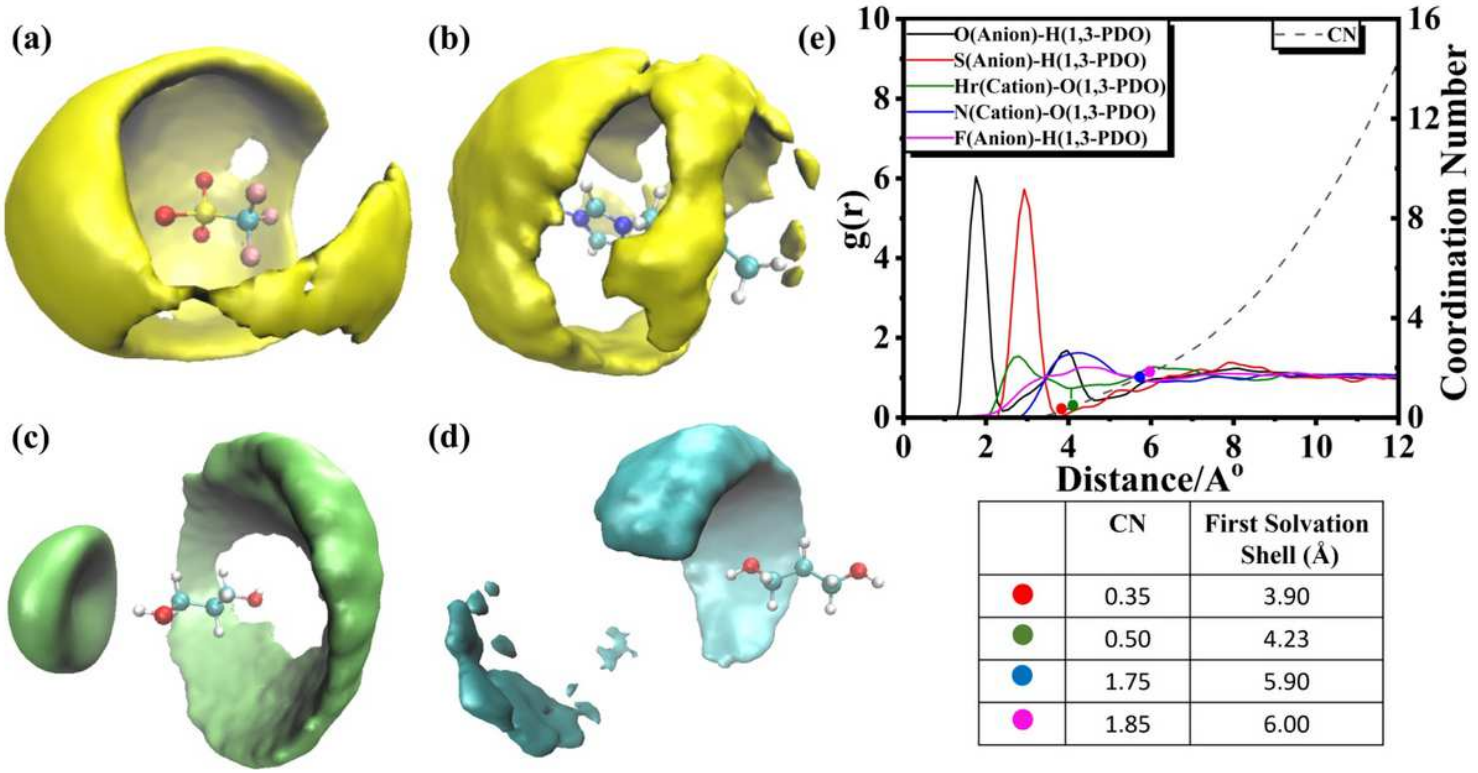

	CN	First Solvation Shell (Å)
●	0.35	3.90
●	0.50	4.23
●	1.75	5.90
●	1.85	6.00

Figure 6

Molecular Distribution Analysis and Interatomic RDF of [Bmim][TFO] with 1,3-PDO. (a) SDF of 1,3-PDO around $[TFO]^-$, (b) SDF of 1,3-PDO around $[Bmim]^+$, (c) SDF of [TFO] around 1,3-PDO, (d) SDF of $[Bmim]^+$ around 1,3-PDO, and (e) Interatomic RDF Plot of ILs and 1,3-PDO at 298 K.

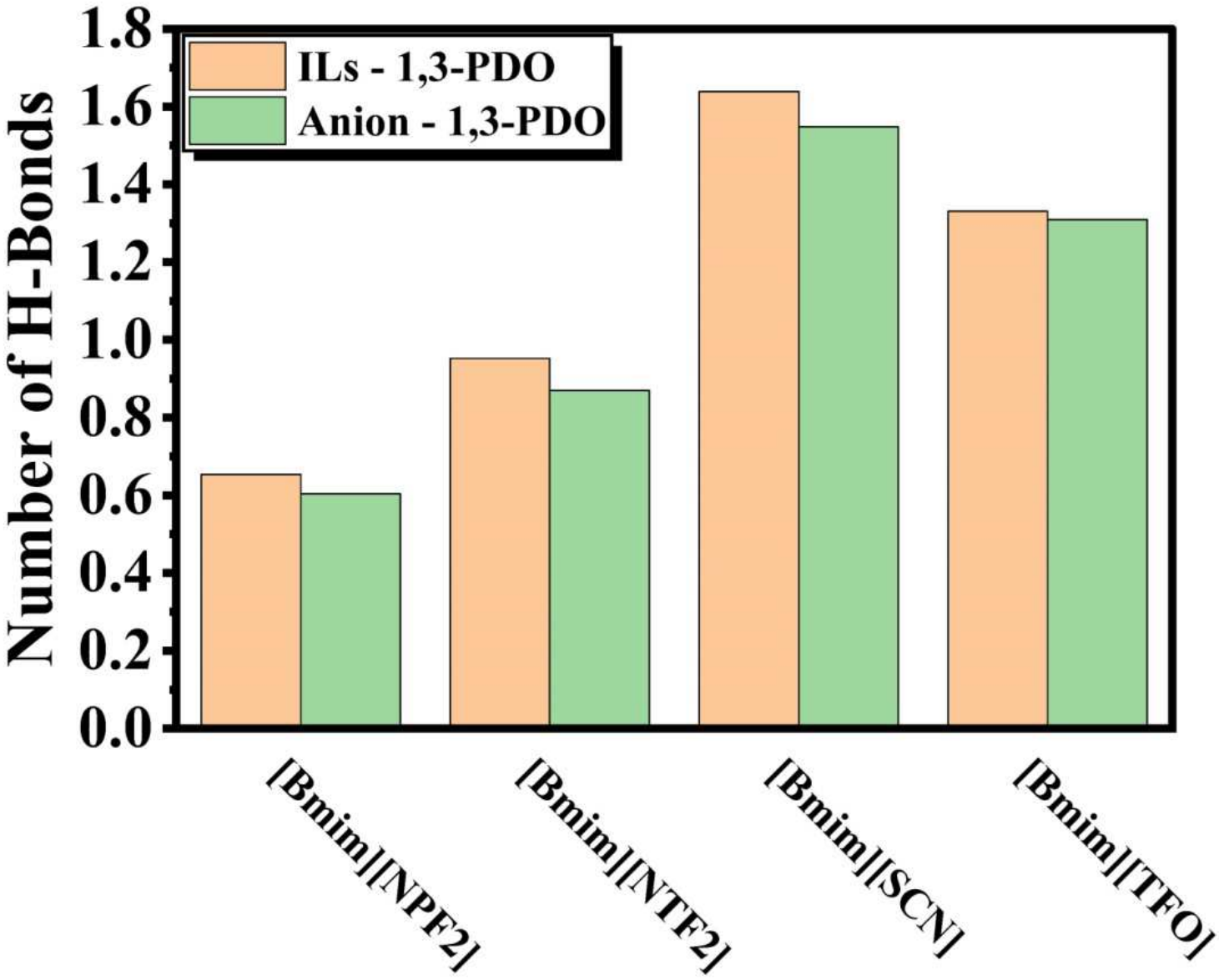

Figure 7

Number of Hydrogen Bonds between Ionic Liquids (ILs) and 1,3-Propanediol (1,3-PDO) per 1,3-PDO.

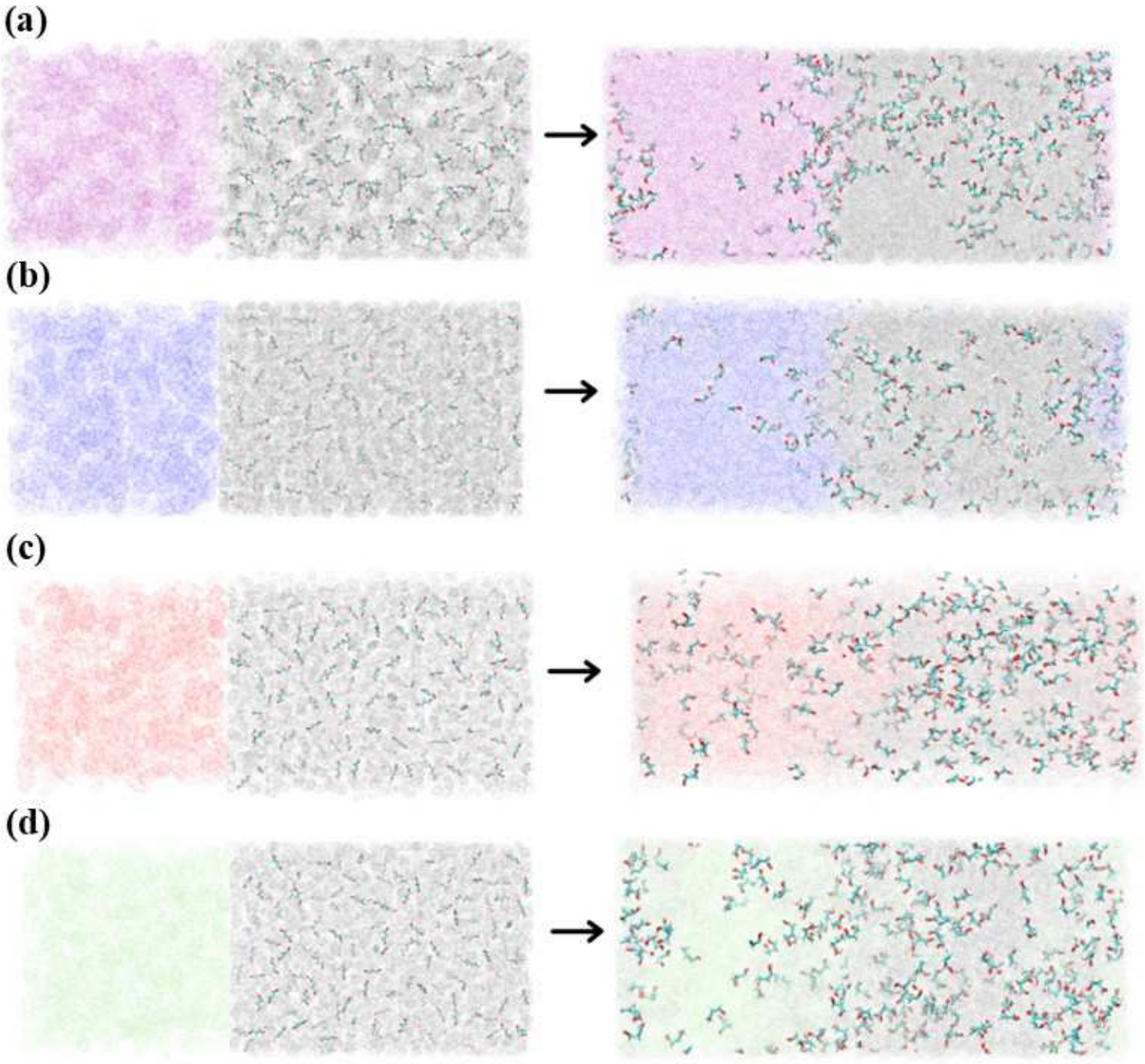

Figure 8

Snapshot of 1,3-PDO Transfer from raffinate phase (aqueous phase) to extract phase (IL phase) during a 30 ns Molecular Dynamics (MD) Simulation at 298 K with distinct colors representing different ILs: [Bmim][NPF2] (purple), [Bmim][NTF2] (blue), [Bmim][SCN] (red), and [Bmim][TFO] (lime), while water is depicted in gray.

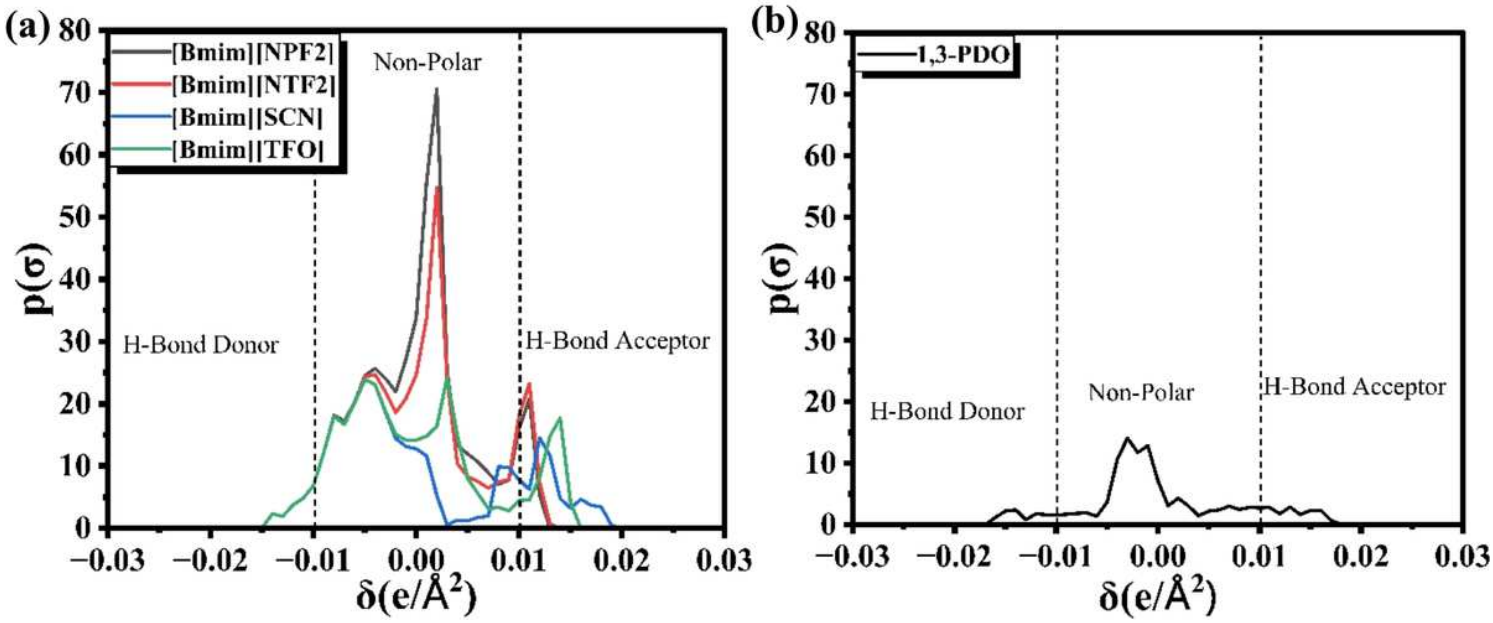

Figure 9

Sigma Profile Histograms for (a) Ionic Liquids (ILs) and (b) 1,3-Propanediol (1,3-PDO) analyzed with COSMO-SAC.

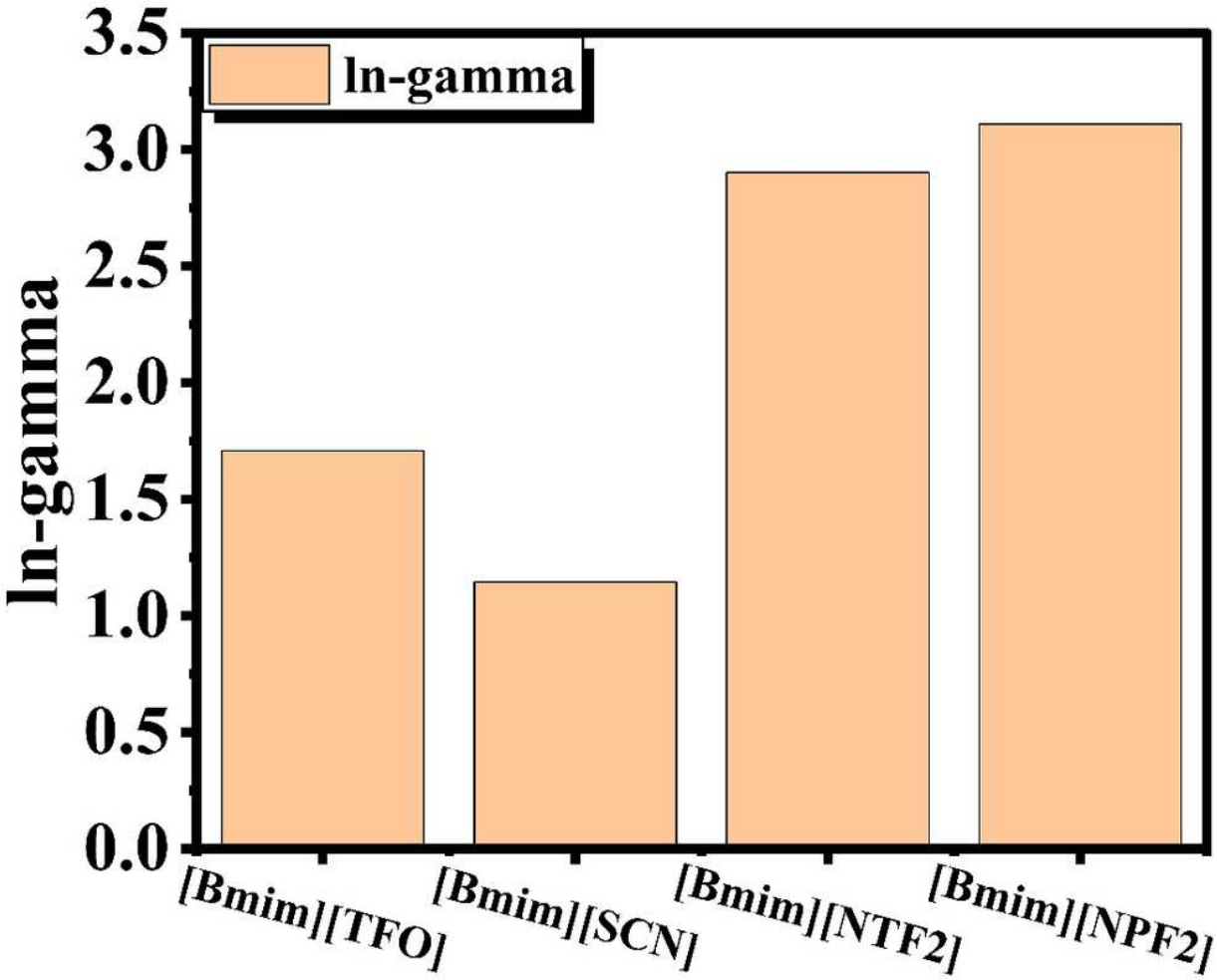

Figure 10

Logarithmic Infinite Dilution Activity Coefficients of 1,3-PDO in Ionic Liquids (ILs).

Supplementary Files

This is a list of supplementary files associated with this preprint. Click to download.

- floatimage1.png
- Tables.docx
- SupplementaryMaterial.docx